Comparison of different interpolation operators including nonlinear subdivision schemes in the simulation of particle trajectories

Bouchra Bensiali[a,*], Kowsik Bodi[a,b], Guido Ciraolo[a,c], Philippe Ghendrih[d], Jacques Liandrat[e,c]

[a] *M2P2, 13451 Marseille, France.*
[b] *Aerospace Engg., IIT Bombay, Mumbai 400076, India.*
[c] *Centrale Marseille, 13451 Marseille, France.*
[d] *CEA, IRFM, 13108 St Paul-Lez-Durance, France.*
[e] *LATP, 13453 Marseille, France.*

Abstract

In this work, we compare different interpolation operators in the context of particle tracking with an emphasis on situations involving velocity field with steep gradients. Since, in this case, most classical methods give rise to the Gibbs phenomenon (generation of oscillations near discontinuities), we present new methods for particle tracking based on subdivision schemes and especially on the Piecewise Parabolic Harmonic (PPH) scheme which has shown its advantage in image processing to reconstruct images with strong contrasts. First an analytic 1D case with a discontinuous velocity field is considered in order to highlight the effect of the Gibbs phenomenon on trajectory calculation and to provide theoretical results. Then, we show, regardless of the interpolation method, the need to use a conservative approach when integrating a conservative problem with a velocity field deriving from a potential. Finally, the PPH scheme is applied in a more realistic case of a time-dependent potential encountered in the edge turbulence of magnetically confined plasmas, to compare the propagation of density structures (turbulence bursts) and the evolution of test particles. This study shows the difference between particle transport and density transport in turbulent fields.

Keywords: interpolation, subdivision schemes, PPH, Gibbs phenomenon, edge plasma, density structures, test particles

1. Introduction

The tracking of particles convected passively in a velocity field is a classical problem in physics but its simulation is often difficult since the velocity field, that usually is itself an output of an Eulerian simulation, is only known on a fixed grid of points [1, 2, 3, 4]. Since the tracking is based on a Lagrangian description of the trajectory of the particle, evaluation of the velocity field on arbitrary points is required.

Evaluation of a field on arbitrary points is required in many studies for instance in fluid dynamics, geostatistics, image compression and, more generally multiscale approximation [5, 6, 7, 8, 9].

Subdivision schemes are nowadays becoming workhorses for advanced scientific computing in data and geometry processing. Among them, some nonlinear schemes based on nonlinear transforms are reaching a recognized status supported by recent results concerning their precision and stability as well as their satisfactory behaviour in presence of strongly varying data (either intrinsic to the problem or due to sampling) where linear schemes, due to the Gibbs phenomenon, generally fail [10].

In this paper we propose a comparison of different tracking algorithms based on different interpolation operators: polynomial interpolation, spectral interpolation and spline interpolation are compared to subdivision operators based on local polynomial interpolation and a nonlinear perturbation of it, called PPH (Piecewise Parabolic Harmonic) subdivision [10]. Our investigations are both theoretical and numerical with applications to univariate and multivariate situations.

The paper is organized as follows: after a detailed presentation of the different interpolation operators in section 2, and a brief recall of the problem of the trajectory evaluation in section 3, the univariate situation is

*Corresponding author. Tel: +33 4 91 11 85 21; Fax: +33 4 91 11 85 02.
Email addresses: bensiali@l3m.univ-mrs.fr (Bouchra Bensiali), kbodi@aero.iitb.ac.in (Kowsik Bodi), ciraolo@l3m.univ-mrs.fr (Guido Ciraolo), philippe.ghendrih@cea.fr (Philippe Ghendrih), jacques.liandrat@centrale-marseille.fr (Jacques Liandrat)

investigated in section 4 with a theoretical analysis of the convergence of the numerical tracking schemes for the different interpolation operators (4.1). Section 5 is devoted to bivariate situations: we start with the comparison between conservative and nonconservative approaches to track particles in a velocity field deriving from a potential. The end of this section is devoted to particle tracking in a turbulent velocity field related to numerical simulations of edge fusion plasma: we investigate in particular the relation between test-particle dynamics and density structures evolution, and it is shown that physical informations of high interest can be reached if suitable interpolation operators are used. The last section is devoted to conclusion and remarks.

2. Numerical methods

In this section, we describe the interpolation methods we use. We first recall classical methods including polynomial, spectral and cubic splines interpolations. Then subdivision schemes are presented with emphasis on the Piecewise Parabolic Harmonic (PPH) scheme. The univariate framework is adopted for the presentation. Bivariate and multivariate applications are derived using a tensor product approach.

We denote by $(f_n)_{0\leq n\leq N}$ the sampling of a function f on a uniform grid $(x_n)_{0\leq n\leq N}$ of an interval $[0,a]$: $x_n = n\delta = n\frac{a}{N}$.

2.1. Classical interpolation methods

Polynomial interpolation

In this paper, we call polynomial interpolation of degree $2p+1$ the classical piecewise centered Lagrange interpolation: in each interval $[x_n, x_{n+1}]$, f is approximated by the unique polynomial P_n of degree $2p+1$ which interpolates $(x_{n-p}, f_{n-p}), ..., (x_{n+p+1}, f_{n+p+1})$.

Introducing, for $-p \leq i \leq p+1$, Lagrange polynomials[1]

$$L_i^n(x) = \prod_{k=-p, k\neq i}^{p+1} \frac{x - x_{n+k}}{x_{n+i} - x_{n+k}},$$

P_n is given by

$$P_n(x) = \sum_{i=-p}^{p+1} f_{n+i} L_i^n(x).$$

Spectral interpolation

Spectral interpolation involves trigonometric polynomials [11]. More precisely, we call spectral interpolation of f relative to the grid $(x_n)_{0\leq n\leq N-1}$ the following trigonometric polynomial of degree N (supposed to be even):

$$T_N(x) = \sum_{k=-N/2}^{N/2-1} \tilde{f}_k \exp(2i\pi kx/a),$$

where $(\tilde{f}_k)_{-N/2\leq k\leq N/2-1}$ stands for the discrete Fourier transform of $(f_n)_{0\leq n\leq N-1}$ defined by

$$\tilde{f}_k = \frac{1}{N} \sum_{n=0}^{N-1} f_n \exp(-2i\pi kn/N),\ k = -N/2, \ldots, N/2-1.$$

Cubic splines

Cubic splines are C^2 continuous, piecewise polynomials of degree 3 interpolating the grid points [12]. Most of the fields considered in this paper are periodic, thus we implemented periodic spline interpolation using the procedure described in Ref. [13].

[1]Note that developing $L_i^n(x_n + r\delta)$ for $r \in [0,1]$, one finds that $L_i^n(x_n + r\delta)$ is independent of n and δ: $L_i^n(x_n + r\delta) = L_i(r)$ or in other words $L_i^n(n\delta_1 + r\delta_1) = L_i^m(m\delta_2 + r\delta_2)$. There is invariance by translation and dilatation.

2.2. Subdivision schemes

Initially introduced for curves and surfaces design, subdivision schemes are now basic elements for computer aided design, computational science, and image processing [14, 10].

The basic ingredient for dyadic stationary and uniform linear interpolant subdivision scheme is an operator in $\ell^\infty(\mathbb{Z})$, the set of bounded sequences, that reads:

$$S : \left\{ \begin{array}{lcl} \ell^\infty(\mathbb{Z}) & \longrightarrow & \ell^\infty(\mathbb{Z}) \\ f = (f_n)_{n\in\mathbb{Z}} & \longmapsto & ((Sf)_n)_{n\in\mathbb{Z}} \end{array} \right. \text{ with } \left\{ \begin{array}{l} (Sf)_{2n} = f_n, \\ (Sf)_{2n+1} = \sum_k a_{2n+1-2k} f_k, \end{array} \right. \tag{1}$$

where $(a_n)_{n\in\mathbb{Z}}$ is a set of null coefficients but a finite number that defines the scheme. Starting from a sequence $f^0 = (f_n^0)_{n\in\mathbb{Z}}$ and defining $f_n^{j+1} = (Sf^j)_n$, $n \in \mathbb{Z}$, $j \in \mathbb{N}$, a convergent subdivision scheme S defines, for all initial sequence f^0, a continuous function f^∞ such that $\lim_{j\to+\infty} \sup_n |f_n^j - f^\infty(x_n^j)| = 0$ where $x_n^j = 2^{-j}x_n = n2^{-j}\delta$.

Making the coefficients $(a_n)_{n\in\mathbb{Z}}$ depend on the position n (respectively the scale j) leads to nonuniform (respectively nonstationary) schemes. Making them dependent of f defines nonlinear subdivision schemes.

In this paper, two convergent subdivision schemes will be used, the Lagrange and the PPH schemes [14, 15]. The first one is a linear scheme whereas the second is nonlinear.

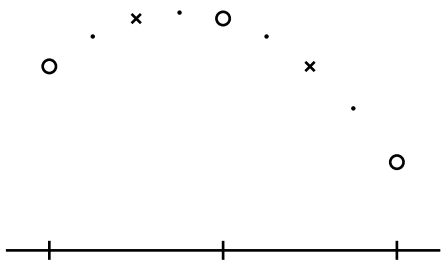

Figure 1: The iteration of a subdivision scheme provides a multiscale method that allows one to approximate a function on a grid finer and finer: starting from the circles corresponding to the values on the initial grid, the crosses represent the first iteration and the dots the second iteration.

Lagrange scheme

Here, on each interval, the new points are defined as the value taken by a polynomial determined by neighbouring previously computed points.

In this paper, we use the degree 3 centered Lagrange interpolation: to define the value of Sf at the midpoint of index $2n+1$, we use the unique cubic polynomial P_n (already defined for polynomial interpolation) that interpolates (x_{n-1}, f_{n-1}), (x_n, f_n), (x_{n+1}, f_{n+1}), and (x_{n+2}, f_{n+2}). More precisely, $(Sf)_{2n+1} = P_n\left(\frac{x_n+x_{n+1}}{2}\right)$. We obtain

$$\left\{ \begin{array}{l} (Sf)_{2n+1} = -\frac{1}{16}f_{n-1} + \frac{9}{16}f_n + \frac{9}{16}f_{n+1} - \frac{1}{16}f_{n+2}, \\ (Sf)_{2n} = f_n. \end{array} \right. \tag{2}$$

This scheme is referred to as a linear scheme because the new points are defined as a linear combination of the old ones. Note that even if the connection with polynomial interpolation is trivial after one iteration, the limit function $S^\infty f^0$ is generally not a piecewise polynomial.

PPH scheme

The PPH scheme is also based on a polynomial interpolation. Introducing the differences $Df_n = f_{n+1} - 2f_n + f_{n-1}$, the polynomial $\bar{P}_n$ used here to define $(Sf)_{2n+1}$ interpolates (x_{n-1}, f_{n-1}), (x_n, f_n), (x_{n+1}, f_{n+1}), and $(x_{n+2}, \bar{f}_{n+2})$ with

$$\bar{f}_{n+2} = f_{n+1} + f_n - f_{n-1} + 2H(Df_n, Df_{n+1}), \tag{3}$$

where H is defined by:

$$H(x,y) = \begin{cases} 2\frac{xy}{x+y}, & \text{if } xy > 0, \\ 0, & \text{otherwise.} \end{cases} \tag{4}$$

The PPH scheme is a perturbation of the Lagrange scheme. Indeed, remarking that $f_{n+2} = f_{n+1} + f_n - f_{n-1} + 2\frac{Df_n + Df_{n+1}}{2}$, it clearly appears that the arithmetic mean of local differences has been substituted by the harmonic mean. Finally, we obtain

$$\begin{cases} (Sf)_{2n+1} = \frac{f_n + f_{n+1}}{2} - \frac{1}{8}H(Df_n, Df_{n+1}), \\ (Sf)_{2n} = f_n. \end{cases} \tag{5}$$

The introduction of the PPH scheme is mainly motivated by the fact that the PPH subdivision does not produce the Gibbs phenomenon (oscillation near discontinuities) while preserving the other good properties of the Lagrange subdivision. Its convergence has been established in [15].

Remark 2.1. *An important aspect for implementation of the interpolation prediction methods is their local/global properties that influence directly their ability to be efficiently parallelized. As mentioned in Table 1, spectral and spline methods are global. The others are local and, for a four point stencil considered here, the prediction at a given position in one dimension involves only the 4 nearest points. There are, moreover, important differences between classical methods and subdivision schemes. While the former allow one to predict f at any position x, the latter only provides the prediction at dyadic points. In addition, the interpolatory function is directly given for classical methods while it is only known as the limit of the convergent subdivision process in the latter situation. These facts have various consequences:*

- *Since subdivision provides only predictions at dyadic points (of the form $k2^{-L}\Delta x$, with L the level of subdivision starting from the initial grid size Δx), an additional error linked to localization is introduced. If $\|f'\|_\infty$ stands for the L^∞ norm of the first derivative of f, then this error is bounded by $2^{-L}\Delta x\|f'\|_\infty$. Therefore, if ε_s stands for a target error,*

$$L > \frac{\log\left(\frac{\Delta x\|f'\|_\infty}{\varepsilon_s}\right)}{\log 2}. \tag{6}$$

  In practice, $\|f'\|_\infty$ is evaluated numerically and ε_s is fixed: formula (6) then gives the number of required subdivision steps for each evaluation.

- *Interpolatory subdivision presented above are based on polynomial interpolation on dyadic points. Therefore, one could wonder what are the advantages of using subdivision rather than the corresponding polynomial interpolation on each point. It turns out to be that the advantages are threefold: first, from a mathematical point of view, as shown in Table 1, the interpolatory function for piecewise polynomial interpolations is C^0 while it is more regular for subdivision. In particular, for the PPH subdivision it is C^{1-} and even C^2 in strictly convex regions. Second, from a computational point of view, four point subdivision involves only the storage of 4 coefficients independent of the subdivision level. Direct polynomial interpolation involves 16 coefficients that are grid dependent. Third, generalization to bivariate configuration such as done in the next sections is straightforward for subdivision using tensorial product. It becomes very costly for piecewise bivariate interpolation.*

Interpolation	Classical method				Subdivision scheme	
	spectral	linear dÂ°1	poly. dÂ°3	spline	Lagrange	PPH
Smoothness	C^∞	C^0 piecewise poly. dÂ°1	C^0 piecewise poly. dÂ°3	C^2 piecewise poly. dÂ°3	C^{2-}	C^{1-}, C^2 (strictly convex data)
Rate of convergence / approximation		2	4	4	4	3
Local / global implementation	global	local	local	local - global (coefficients)	local	local
Gibbs phenomenon	yes	no	yes	yes	yes	no

Table 1: Some properties of the interpolation methods.

3. Trajectory evaluation

Now that the interpolation schemes have been introduced, we address the problem of trajectory evaluation. The general problem we are interested in is the computation of the trajectory $\mathbf{X}(t)$ of a particle swept along by a velocity field $\mathbf{F}$ following the equation:

$$\begin{cases} \dot{\mathbf{X}} = \mathbf{F}(\mathbf{X}, t), & t \in [t_0, T], \\ \mathbf{X}(t_0) = \mathbf{X}_0, \end{cases} \tag{7}$$

where $\mathbf{F}(\mathbf{X}, t)$ is supposed to be known on a regular grid. Any numerical resolution of (7) involves the evaluation of $\mathbf{F}$ on arbitrary points and therefore requires interpolation operators.

Although in this paper we focus on particle trajectories, the framework of the methods discussed here is more general and may relate to problems of propagation of fronts, shock waves or passive tracers.

In the following sections, we aim to study situations involving strongly varying velocity fields $\mathbf{F}$. We consider first an analytic univariate case with a discontinuous velocity field in order to provide theoretical results, then a more realistic case dealing with test particle transport in a magnetized plasma is considered.

4. Univariate case

When used to reconstruct a discontinuous function, most classical methods of interpolation or approximation give rise to the Gibbs phenomenon which is characterized by the generation of oscillations near discontinuities. In this section, we highlight the effect of the Gibbs phenomenon on trajectory calculation. In our framework of particle tracking, the Gibbs phenomenon may lead to incorrect trajectories.

4.1. Steady state velocity field

Here we consider (7) with a velocity field F exhibiting a discontinuity of amplitude $d > 0$ given by

$$F(x,t) = v(x) = \begin{cases} 0.5, & \text{if } x < 0.5, \\ 0.5 + d = v_p, & \text{if } x \geq 0.5, \end{cases} \tag{8}$$

and focus on the initial condition $x_0 = 0.2$ at $t_0 = 0$.

4.1.1. Analytical integration

4.1.1.1. Mathematical meaning of the differential equation. It should be noted that the right-hand side (8) of the differential equation (7) being discontinuous, the classical definition of a solution of a differential equation with a continuous right-hand side, as a function which has a derivative and satisfies the equation everywhere on a given interval, is no longer valid. *A fortiori*, the Cauchy-Lipschitz theorem [16] ensuring the existence and the uniqueness of the solution does not apply.

One can propose, however, a good candidate to be solution of the Cauchy problem (7) for the velocity v given by (8). It is the connection, at $x = 0.5$, of two classical solutions:

$$x(t) = \begin{cases} 0.2 + 0.5t, & \text{if } t < 0.6, \\ 0.5 + v_p(t - 0.6), & \text{if } t \geq 0.6. \end{cases} \tag{9}$$

For $t = 0.6$, the derivative of the function defined by (9) does not exist, thus the equation (7) is not satisfied at $t = 0.6$ in the traditional sense. However, the function (9) is the unique solution of the integral formulation[2]

$$x(t) = x_0 + \int_0^t v(x(s))ds. \tag{10}$$

One should remark however that the integral formulation is not always sufficient to provide a reasonable rigorous meaning to a differential equation with a discontinuous right-hand side. To illustrate this point, let us consider the following right-hand side [17]

$$v(x) = 1 \quad \text{if } x < 0.5, \quad v(0.5) = a \neq 0, \quad v(x) = -1 \quad \text{if } x > 0.5. \tag{11}$$

[2]The integral formulation is equivalent to the differential equation in the case of a continuous right-hand side: a solution of a differential equation subject to an initial condition is a solution of the corresponding integral formulation and *vice versa*.

For $x > 0.5$, the solutions are $x(t) = -t + c_1$, and for $x < 0.5$, the solutions are $x(t) = t + c_2$. When t increases, the solutions reach the line $x = 0.5$. The field forbids to cross the axis $x = 0.5$. And the problem is to find a definition which gives a meaning to the constant solution $x(t) = 0.5$. The classical sense is unsurprisingly eliminated, since for this constant solution $\dot{x} = 0$, whereas the right hand-side is nonzero at $x = 0.5$. The integral formulation does not fix the problem here because it requires $a = 0$ through

$$x(t) = 0.5 = 0.5 + \int_0^t v(x(s))ds = 0.5 + at. \tag{12}$$

The consideration of differential equations with discontinuous right-hand side then requires the generalization of the concept of solution. Different approaches have been proposed [17, 18]. However it is out of the scope of this paper, and we adopt the formulations (9) or (10) that fit to (7)-(8).

4.1.1.2. Convergence of the Euler scheme to the solution. Given a fixed time step Δt, we note $t_n = n\Delta t$ and y_n the calculated position at time t_n. Using the explicit Euler scheme we have

$$y_n = \begin{cases} x_0 + 0.5n\Delta t, & \text{if } n \leq n_0 \ (n_0 \text{ s.t. } n_0 - 1 < \frac{0.5-x_0}{0.5\Delta t} \leq n_0), \\ y_{n_0} + v_p(n - n_0)\Delta t, & \text{if } n \geq n_0 + 1. \end{cases} \tag{13}$$

We get that $\sup_n |y_n - x(n\Delta t)| \xrightarrow[\Delta t \to 0]{} 0$ that is the convergence of the scheme.

4.1.2. Integration using interpolation methods

Here, we consider that the velocity v is only known on a uniform grid of step $h = \Delta x$ (we consider a grid that contains the discontinuity point) and that an interpolation method is used to reconstruct the velocity everywhere.

If we denote by $v_{h,\text{interp}}$ the reconstruction obtained using the interpolation method under consideration, then the estimation of the particle trajectory by the interpolation method is given by the integration of

$$\begin{cases} \dot{x} = v_{h,\text{interp}}(x), & t \in [0, T], \\ x(0) = x_0. \end{cases} \tag{14}$$

Two interpolation methods are compared: PPH subdivision, which coincides here with linear interpolation (polynomial interpolation of degree 1) and for which there is no Gibbs phenomenon, and polynomial interpolation of degree 3, suffering from the Gibbs phenomenon, see Fig. 2.

In (14), unlike the initial equation (7)-(8), the right-hand side term is a continuous function which verifies the conditions of the Cauchy-Lipschitz theorem, thus there exists a unique solution of the Cauchy problem, denoted $x_{h,\text{interp}}$.

Reconstruction of the velocity.

PPH interpolation.

$$v_{h,\text{pph}}(x) = \begin{cases} 0.5, & \text{if } x \leq 0.5 - h, \\ 0.5\frac{x-0.5}{-h} + v_p\frac{x-(0.5-h)}{h} = \frac{d}{h}x + v_p - \frac{d}{h}0.5, & \text{if } 0.5 - h \leq x \leq 0.5, \\ v_p, & \text{if } x \geq 0.5. \end{cases} \tag{15}$$

Polynomial interpolation.

$$v_{h,\text{poly}}(x) = \begin{cases} 0.5, & \text{if } x \leq 0.5 - 2h, \\ P_1(x), & \text{if } 0.5 - 2h \leq x \leq 0.5 - h, \\ P_2(x), & \text{if } 0.5 - h \leq x \leq 0.5, \\ P_3(x), & \text{if } 0.5 \leq x \leq 0.5 + h, \\ v_p, & \text{if } x \geq 0.5 + h. \end{cases} \tag{16}$$

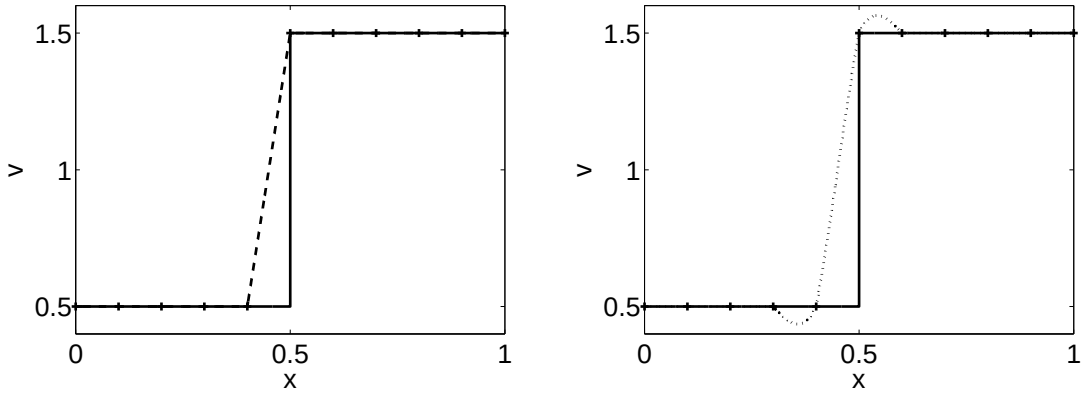

(a) (b)

Figure 2: Exact velocity field (solid line) given by Eq. (8) with $d = 1$, and approximations by (a): PPH scheme (dashed line) and (b): polynomial interpolation of degree 3 (dotted line) for $h = 0.1$.

4.1.3. Convergence

4.1.3.1. Convergence of the reconstruction. For both interpolation methods, $v_{h,\text{interp}}$ converges uniformly to v when h tends to 0 on any closed interval not containing the discontinuity point 0.5.

4.1.3.2. Convergence of the trajectory. For PPH interpolation (and linear interpolation), the solution of the problem (14) can be computed explicitly. We find for h small enough (such that at $t = 0$, $v_h(x_0) = v_h(0.2) = v(0.2) = 0.5$):

$$x_{h,\text{pph}}(t) = \begin{cases} 0.2 + 0.5t, & \text{if } 0 \le t \le \frac{0.3-h}{0.5} = t_1, \\ (\frac{v_p}{d} - 1)h \exp\left(\frac{d}{h}(t - t_1)\right) + (0.5 - \frac{v_p}{d}h), & \text{if } t_1 \le t \le \frac{h}{d} \ln\left(\frac{v_p}{v_p - d}\right) + t_1 = t_2, \\ 0.5 + v_p(t - t_2), & \text{if } t \ge t_2. \end{cases} \tag{17}$$

One obtains immediately the convergence of the solution $x_{h,\text{pph}}$ to the exact solution (9) of the initial problem (with discontinuous right-hand side) when the discretization step h tends to 0.

In the case of polynomial interpolation, the explicit calculation of the solution is not possible in general. However, a counterexample to the convergence of $x_{h,\text{poly}}$ to the exact solution x can be found without calculating the solution. Indeed, the polynomial interpolation and the Lagrange scheme coincide at the midpoints of the initial grid, it follows using (2)

$$\begin{aligned} v_{h,\text{poly}}(0.5 - 3h/2) &= -\frac{1}{16}0.5 + \frac{9}{16}0.5 + \frac{9}{16}0.5 - \frac{1}{16}v_p, \\ &= \frac{17}{16}0.5 - \frac{1}{16}v_p, \\ &= 0.5 - \frac{1}{16}(v_p - 0.5), \\ &= 0.5 - \frac{1}{16}d, \end{aligned} \tag{18}$$

where d is the jump at the discontinuity point.

Thus, the value of the reconstruction at the considered midpoint is a constant c that does not depend on the step $h = \Delta x$, but only on d the amplitude at the discontinuity point. The oscillation generated in the reconstruction of v using polynomial interpolation then remains despite the reduction of h, it is the Gibbs phenomenon.

If we take, for instance, $d = 16$, then the constant c is negative. By continuity of $v_{h,\text{poly}}$, we deduce, using the intermediate value theorem, the existence of a point x^0 (depending on h) in $[0.5 - 2h, 0.5 - 3h/2]$ where $v_{h,\text{poly}}(x^0) = 0$.

For a fixed h, the constant function $X(t) = x^0$ is solution of the differential equation $\dot{x} = v_{h,\text{poly}}(x)$ subject to the initial condition $x(0) = x^0$. Thus using Cauchy-Lipschitz theorem, we have for $h > 0$ small enough (such that $x^0 \ge 0.5 - 2h > 0.2 = x_0$)

$$\forall t \ge 0, \quad x_{h,\text{poly}}(t) < x^0 < 0.5 - 3h/2 < 0.5, \tag{19}$$

and this proves that if $x_{h,\text{poly}}$ converges to x_{poly} as h approaches 0, then passing to the limit in (19), we get that $x_{\text{poly}}(t) \leq 0.5$ for all $t \geq 0$, and $x_{\text{poly}} \neq x$ the exact solution (9) of the initial problem (7)-(8).

Fig. 3 illustrates the convergence result in the case $d = 16$: the trajectory $x_{h,\text{pph}}$ converges to the exact trajectory when the step h tends to 0 contrary to the trajectory $x_{h,\text{poly}}$ which remains bounded by $x = 0.5$.

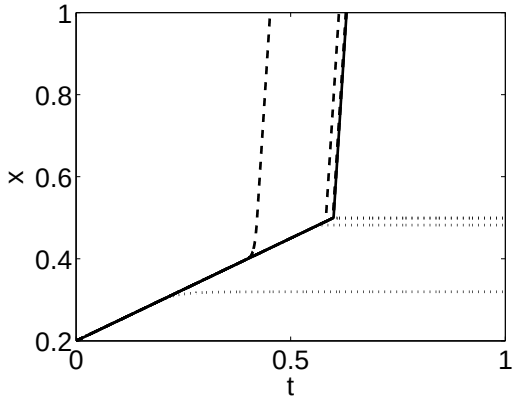

Figure 3: Plots of $x_{h,\text{pph}}$ (dashed line) and $x_{h,\text{poly}}$ (dotted line) solutions of the Cauchy problem (14) with $x_0 = 0.2$ for the velocity v given by (8) with $d = 16$, and h varying from 10^{-1} to 10^{-4}. The variation of $x_{h,\text{pph}}$, respectively $x_{h,\text{poly}}$, as h decreases, is from left to right, respectively from bottom to top. The exact trajectory (9) is shown in solid line.

Remark: In practice, we stop after a number of iterations L when the PPH scheme is used, which provides a sequence of values corresponding to the refined grid. Then, one can use a piecewise constant approximation to define $v_{h,\text{pph},L}$ and consider the trajectory $x_{h,\text{pph},L}$ solution of $\dot{x} = v_{h,\text{pph},L}(x)$, $x(0) = x_0$ under integral formulation. One can write $v_{h,\text{pph},L}(x) = v_{h,\text{pph}}(x) + \varepsilon_{h,L}(x)$ with $|\varepsilon_{h,L}(x)| \leq \varepsilon_L$ (where $\varepsilon_L = \frac{d}{2^L}$ for example). Setting $y = x_{h,\text{pph}}$ and $z = x_{h,\text{pph},L}$ for simplicity, we obtain $z(t) - y(t) = \int_0^t \left((v_{h,\text{pph}}(z(s)) - v_{h,\text{pph}}(y(s))) + \varepsilon_{h,L}(z(s)) \right) ds$. Thus for $t \geq 0$,

$$\begin{aligned} |z(t) - y(t)| &\leq \int_0^t \left| v_{h,\text{pph}}(z(s)) - v_{h,\text{pph}}(y(s)) \right| ds + \int_0^t \left| \varepsilon_{h,L}(z(s)) \right| ds \\ &\leq k \int_0^t |z(s) - y(s)| \, ds + \varepsilon_L t, \end{aligned} \tag{20}$$

using the Lipschitz continuity of $v_{h,\text{pph}}$ for $h > 0$ ($k \geq 0$ being a Lipschitz constant for $v_{h,\text{pph}}$) and $|\varepsilon_{h,L}(x)| \leq \varepsilon_L$. Using now the Gronwall's lemma, one obtains $|x_{h,\text{pph},L}(t) - x_{h,\text{pph}}(t)| = |z(t) - y(t)| \leq \varepsilon_L t \exp(kt)$ for $t \geq 0$ and $\lim_{L\to\infty} x_{h,\text{pph},L} = x_{h,\text{pph}}$. It follows $\lim_{h\to 0} \lim_{L\to\infty} x_{h,\text{pph},L} = x$ where x is the exact trajectory of the initial problem (7)-(8).

4.1.3.3. Specific convergence analysis when Δt is related to h. The previous section was devoted to the convergence of the numerical trajectory towards the real trajectory when the step h defining the sampling of v goes to zero and according to the different reconstruction procedure analyzed in this paper. More precisely,

$$\text{constructing } (x_{n,h})_{n\in\mathbb{N}} \text{ as: } x_{0,h} = x_0,\ x_{n+1,h} = x_{n,h} + \Delta t\, v_h(x_{n,h}) \text{ and } x_h = \lim_{\Delta t\to 0}(x_{n,h}), \text{ what is } \lim_{h\to 0} x_h? \tag{21}$$

Now we would like to investigate a situation where the time step Δt used for the evaluation of $(x_{n,h})_{n\in\mathbb{N}}$ is related to h, the sampling step of v. This situation mimics the case of a non stationary velocity field solution of an advection equation resolved numerically under the constraint of a so called CFL condition. If we suppose for instance that this condition gives $\Delta t = h$, then the convergence problem is the analysis of $\lim_{\Delta t\to 0}(x_{n,\Delta t})$ if

$$x_{n+1,\Delta t} = x_{n,\Delta t} + \Delta t\, v_{\Delta t}(x_{n,\Delta t}). \tag{22}$$

In the case of PPH interpolation (and linear interpolation), explicit calculation of the terms of the sequence gives the convergence of the solution $x_{\Delta t,\text{pph}}$ to the exact solution (9) of the initial problem (7)-(8) when Δt goes to 0.

For polynomial interpolation with $d = 16$, the reconstructed velocity takes negative values, that leads to nonconvergence to the exact solution in the sense (21). At the discrete level (22), however, this argument is not sufficient to determine whether or not convergence occurs, because it depends on the location of the values of the sequence.

Based on numerical tests performed using time steps 0.1, 0.01 (see Fig. 4), we note that $x_{\Delta t,\mathrm{poly}}$ ends up oscillating between two values.

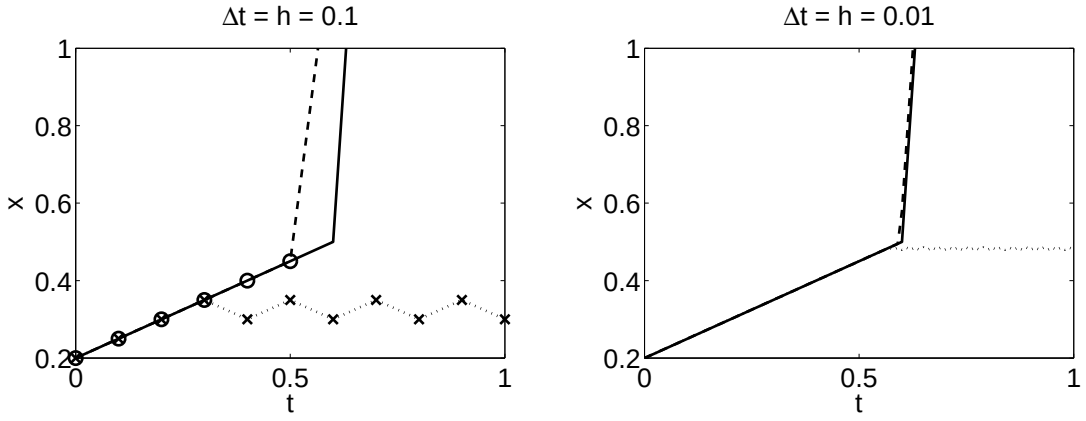

(a) (b)

Figure 4: Plots of $x_{\Delta t,\mathrm{pph}}$ (dashed line) and $x_{\Delta t,\mathrm{poly}}$ (dotted line) given by (22) with $x_0 = 0.2$, for the velocity v given by (8) with $d = 16$, for (a): $\Delta t = 0.1$ and (b): $\Delta t = 0.01$. The exact trajectory (9) is shown in solid line.

We prove this result: for Δt small enough, we have $x_n = 0.2 + 0.5n\Delta t$, as long as $x_{n-1} \leq 0.5 - 2\Delta t$, i.e. as long as $n \leq \frac{0.5-2\Delta t-0.2}{0.5\Delta t} + 1$, that is, for $n \leq n_0$ with $n_0 = \left[\frac{0.6}{\Delta t} - 3\right]$. If we restrict ourselves to $\Delta t = 10^{-k}$, we get $n_0 = 6 \times 10^{k-1} - 3$.

We have $x_{n_0} = 0.2 + 0.5n_0\Delta t$ and for $\Delta t = 10^{-k}$, we get

$$x_{n_0} = 0.5 - 1.5\Delta t, \tag{23}$$

x_{n_0} is exactly the midpoint of $[0.5 - 2\Delta t, 0.5 - \Delta t]$, where the velocity does not depend on Δt (cf. (18)):

$$x_{n_0+1} = x_{n_0} + \Delta t\, v_{\Delta t}(x_{n_0}) = 0.5 - 1.5\Delta t + \Delta t \left(0.5 - \frac{d}{16}\right). \tag{24}$$

The choice $d = 16$ (arbitrary until now) gives $x_{n_0+1} = 0.5 - 2\Delta t$ and

$$x_{n_0+2} = x_{n_0+1} + 0.5\Delta t = 0.5 - 1.5\Delta t = x_{n_0}. \tag{25}$$

It is seen from (24) that choosing $d = 8$ would have given a fixed point, while other options would not have allowed to conclude.

Remark 4.1. *As soon as the polynomial interpolation remains strictly positive (the case $d = 1$ for example), one can show that there is convergence of the trajectory deduced by polynomial interpolation to the exact trajectory (at the continuous level* (21)*, and at the discrete level* (22)*).*

4.2. Time dependent velocity field

We now consider a nonstationary velocity field V given by

$$V(x,t) = v(x - \alpha t), \tag{26}$$

where v is given by Eq. (8) and the corresponding Cauchy problem

$$\begin{cases} \dot{x} = V(x,t) = v(x - \alpha t), \quad t \in [0,T], \\ x(0) = x_0. \end{cases} \tag{27}$$

This time dependent case is a steady state case if one works in the reference frame moving with the velocity: changing the variable x to $y = x - \alpha t$ in (27) gives indeed:

$$\begin{cases} \dot{y} = v(y) - \alpha = w(y), \quad t \in [0, T], \\ y(0) = x_0. \end{cases} \tag{28}$$

The velocity w is nothing but the velocity v shifted downward by a quantity α. Similarly to the steady state case, there is existence and uniqueness of the solution y to the differential equation (28) under the integral formulation, if $w > 0$, that is if $0.5 > \alpha$. Consequently, there is existence and uniqueness of the solution x to (27) if $0.5 > \alpha$.

The corresponding problem using interpolation methods reads

$$\begin{cases} \dot{x} = v_{h,\text{interp}}(x - \alpha t), \quad t \in [0, T], \\ x(0) = x_0, \end{cases} \tag{29}$$

and one can find d and α such that the solution $x_{h,\text{poly}}$ of the problem (29) with $v_{h,\text{interp}} = v_{h,\text{poly}}$, does not converge to the exact solution x. This holds when $w_{h,\text{poly}}(0.5 - 3h/2) = w_0 - \frac{1}{16}d = v_0 - \alpha - \frac{1}{16}d < 0$ that is when $v_0 - \frac{1}{16}d < \alpha$. In particular, the value $d = 1$ for which there was convergence of the polynomial interpolation in the steady state case, can lead to nonconvergence in the time dependent case if $0.4375 < \alpha < 0.5$.

Through this 1D case, we highlighted the negative impact that may be caused by the Gibbs phenomenon on the calculation of trajectories. Admittedly, the considered case is rather extreme because it deals with a discontinuous velocity, but in practice we are confronted with a fixed step h which corresponds to a resolution generally poor, and at this level, strong gradients and discontinuities cannot be discriminated. The comparison made above between PPH subdivision and polynomial interpolation is a special case of the comparison between a method without Gibbs phenomenon and a method with Gibbs phenomenon, the same behaviour is expected for the other methods. In addition, this section shows the advantage of the PPH scheme to calculate trajectories: even if both linear interpolation and PPH scheme avoid the Gibbs phenomenon, the PPH scheme has better properties than linear interpolation, see Tab. 1.

5. Bivariate case

We now consider the evolution of test particles in a 2D potential field. The equations of motion read

$$\begin{pmatrix} \dot{x} \\ \dot{y} \end{pmatrix} = \begin{pmatrix} -\partial_y \phi(x, y, t) \\ \partial_x \phi(x, y, t) \end{pmatrix}, \tag{30}$$

where ϕ is a potential. Following Ref. [19] we consider, as a first example, the following explicit form of the potential:

$$\phi(x, y, t) = \frac{a}{2\pi} \sum_{\substack{n,m=1 \\ n^2+m^2 \leq N^2}}^{N} \frac{\sin(2\pi(nx + my) + \varphi_{nm} - \omega t)}{(n^2 + m^2)^{3/2}}, \tag{31}$$

where φ_{nm} and ω are fixed. In what follows, we choose $N = 25$ and $a = 0.5$. The quantities φ_{nm} are random phases in $[0, 2\pi]$. Fig. 5 shows a visualization of the potential at $t = 0$.

5.1. Steady state potential

Here we consider an autonomous potential $\phi(x, y, t) = \phi(x, y)$ corresponding to $\omega = 0$. The equations of motion are then

$$\begin{pmatrix} \dot{x} \\ \dot{y} \end{pmatrix} = \begin{pmatrix} -\partial_y \phi(x, y) \\ \partial_x \phi(x, y) \end{pmatrix}. \tag{32}$$

From the equations of motion (32), we deduce that

$$\frac{d\phi}{dt} = \partial_x \phi \, \dot{x} + \partial_y \phi \, \dot{y} = 0 \tag{33}$$

along the trajectory, that means that the trajectories live on isopotential surfaces. In particular, the trajectory of a particle located on a closed isopotential line is expected to be closed.

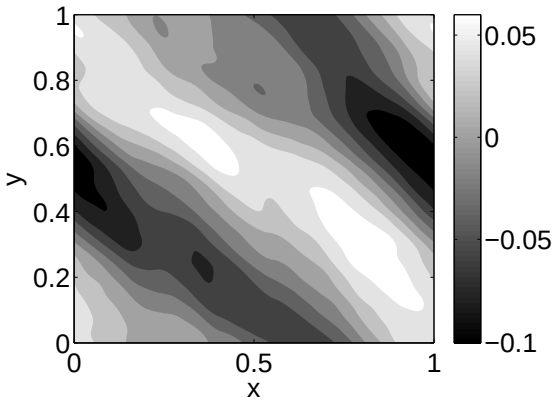

Figure 5: Contour plot of $\phi(x, y, t)$ given by Eq. (31) for $t = 0$, $a = 1$, and $N = 25$.

This system is referred to as a Hamiltonian system where $H = \phi$ is the Hamiltonian. Hamiltonian systems possess specific properties [20, 21, 22]. The Jacobian matrix associated with the system is

$$J = \begin{pmatrix} -\frac{\partial^2 \phi}{\partial x \partial y} & -\frac{\partial^2 \phi}{\partial y^2} \\ \frac{\partial^2 \phi}{\partial x^2} & \frac{\partial^2 \phi}{\partial y \partial x} \end{pmatrix}. \tag{34}$$

The Jacobian matrix appears when one looks at the separation in the phase space of two initially close trajectories: the differences δx and δy between the two trajectories in the x and the y directions respectively satisfy the equations

$$\begin{pmatrix} \dot{\delta x} \\ \dot{\delta y} \end{pmatrix} = J \begin{pmatrix} \delta x \\ \delta y \end{pmatrix}, \tag{35}$$

called the tangent dynamics equations.

The eigenvalues of the matrix satisfy

$$-\left(\frac{\partial^2 \phi}{\partial x \partial y} + \lambda\right)\left(\frac{\partial^2 \phi}{\partial y \partial x} - \lambda\right) + \frac{\partial^2 \phi}{\partial x^2}\frac{\partial^2 \phi}{\partial y^2} = \lambda^2 - \left(\frac{\partial^2 \phi}{\partial x \partial y}\right)^2 + \frac{\partial^2 \phi}{\partial x^2}\frac{\partial^2 \phi}{\partial y^2} = 0, \tag{36}$$

and $\lambda_1 + \lambda_2 = 0$, this is the property of phase space volume conservation for a Hamiltonian system. This last property can also be established noting that $\lambda_1 + \lambda_2 = \mathrm{tr}(J) = -\frac{\partial^2 \phi}{\partial x \partial y} + \frac{\partial^2 \phi}{\partial y \partial x} = 0$.

5.1.1. Application of interpolation methods: different versions

Given the form of the velocity field in the equations (32), there are different ways to apply the interpolation methods: one can either approximate $\partial_x \phi$ and $\partial_y \phi$ on the grid points and then interpolate them or interpolate ϕ and then approximate $\partial_x \phi$ and $\partial_y \phi$. This leads to two versions that do not share the same properties:

Version 1: Approximation of $\partial_x \phi$ and $\partial_y \phi$ on the initial grid and then interpolation

This version consists, after approximation of the derivatives by finite differences (we call $\frac{\Delta \Phi}{\varepsilon_x}$ and $\frac{\Delta \Phi}{\varepsilon_y}$ these approximations) in integrating

$$\begin{pmatrix} \dot{x} \\ \dot{y} \end{pmatrix} = \begin{pmatrix} -(\frac{\Delta \Phi}{\varepsilon_y})_{\mathrm{interp}}(x, y) \\ (\frac{\Delta \Phi}{\varepsilon_x})_{\mathrm{interp}}(x, y) \end{pmatrix}. \tag{37}$$

The discrete Jacobian matrix associated with the system is

$$J_1 = \begin{pmatrix} -\frac{\Delta[(\frac{\Delta \Phi}{\varepsilon_y})_{\mathrm{interp}}]}{\varepsilon_x} & -\frac{\Delta[(\frac{\Delta \Phi}{\varepsilon_y})_{\mathrm{interp}}]}{\varepsilon_y} \\ \frac{\Delta[(\frac{\Delta \Phi}{\varepsilon_x})_{\mathrm{interp}}]}{\varepsilon_x} & \frac{\Delta[(\frac{\Delta \Phi}{\varepsilon_x})_{\mathrm{interp}}]}{\varepsilon_y} \end{pmatrix}. \tag{38}$$

Because in general $\mathrm{tr}(J_1) \neq 0$, the Hamiltonian structure is broken and the conservative property is not guaranteed.

Version 2: interpolation of ϕ and then approximation of $\partial_x\phi$ and $\partial_y\phi$.

This second version consists in integrating

$$\begin{pmatrix}\dot{x}\\ \dot{y}\end{pmatrix} = \begin{pmatrix}-\frac{\Delta\Phi_{\text{interp}}}{\varepsilon_y}(x,y)\\ \frac{\Delta\Phi_{\text{interp}}}{\varepsilon_x}(x,y)\end{pmatrix}. \tag{39}$$

This version is "conservative": indeed a direct computation of $\Phi_{\text{interp}}(x_{n+1}, y_{n+1})$ shows that this quantity is asymptotically conserved at each step (i.e. when ε_x, ε_y, Δt go to zero) and therefore remains almost constant on the trajectories. One should notice that the form (39) is moreover required to use symplectic schemes suited to Hamiltonian systems.

Remark 5.1. *In practice, for version 1, the generation of the two sets $\frac{\Delta\Phi}{\varepsilon_x}$ and $\frac{\Delta\Phi}{\varepsilon_y}$ is first performed using interpolation on a fine grid. Then interpolation at each position is performed on the two sets.*

For version 2, interpolation methods are first used to evaluate the potential at each position. The quantities $\frac{\Delta\Phi_{\text{interp}}}{\varepsilon_x}$ and $\frac{\Delta\Phi_{\text{interp}}}{\varepsilon_y}$ are then evaluated. These evaluations involve extra interpolations on a fine grid in the vicinity of each position. This extra interpolation is very expensive for classical interpolation methods but has a negligible cost for subdivision.

The aim of the next two parts is to show the advantage of the conservative version; tests are made in the steady state case. Two criteria of trajectory quality are suggested in order to measure the performance of the methods: potential conservation and Lagrangian statistics.

5.1.2. Potential conservation along the trajectory

Here, interpolation methods are applied using coarse grids of size $\Delta x = \Delta y = \frac{1}{32}$. Tab. 2 summarizes the various parameters used. The time integration is performed using a fourth-order Runge-Kutta scheme (we chose $\Delta t = \frac{\Delta x}{6}$).

Interpolation	Classical method			Subdivision scheme	
	polynomial degree 3	spectral	cubic splines	Lagrange	PPH
Parameters v1	–	–	–	$r = 2^{-22}$	$r = 2^{-22}$
Parameters v2	$\varepsilon_x = \varepsilon_y = 2^{-17}$	$\varepsilon_x = \varepsilon_y = 2^{-17}$	$\varepsilon_x = \varepsilon_y = 2^{-17}$	$r = 2^{-16}$	$r = 2^{-16}$

Table 2: Parameters of the interpolation methods. r: final resolution of the grid after application of a subdivision scheme, $\varepsilon = \varepsilon_x = \varepsilon_y$: used step to approximate derivatives by finite differences. We imposed $2\varepsilon = r$.

Fig. 6 shows the trajectories obtained using polynomial interpolation. One can already note that the conservative version (version 2) provides closed trajectories unlike version 1. Qualitatively, with the conservative method, the closed trajectories do not dissipate and energy is better conserved, whereas with the nonconservative version, the thickness of the curves expected to be closed shows that there is dissipation of energy over time. The same behaviour is observed for the other methods. For instance, Fig. 7 represents the trajectories obtained for a selected particle by the PPH scheme: using the conservative version we obtain a closed trajectory, while with the nonconservative version, the energy dissipates as shown on the one hand by the trajectory which is arranged in a spiral-shape and on the other hand by the x-coordinate which oscillates with a decrease in the amplitude. This is very visible on Fig. 7 and the conservative trajectory is a little different from the exact one. This is more especially visible as the grid is coarse.

At the same time, we have plotted in Fig. 8(a) the variation $\Delta\phi = \phi(t) - \phi(0)$ of the potential along each trajectory: the exact one, the one obtained using PPH version 1, and that obtained using PPH version 2. As expected, the exact potential is conserved along the exact trajectory while it varies along the trajectory obtained by conservative interpolation (version 2) but remains centered around 0 in contrast to its variation along the trajectory obtained by nonconservative interpolation (version 1). And finally in Fig. 8(b), we have plotted the variation $\Delta\phi_{\text{interp}} = \phi_{\text{interp}}(t) - \phi_{\text{interp}}(0)$ of the interpolated potential along each trajectory. In this case, the roles are exchanged and the interpolated potential is conserved along the trajectory obtained using the conservative version as intended.

Focusing now on a particular initial condition, we look at the conservation of the potential along the trajectories obtained by the different interpolation methods using the conservative version. Again, we can look at the

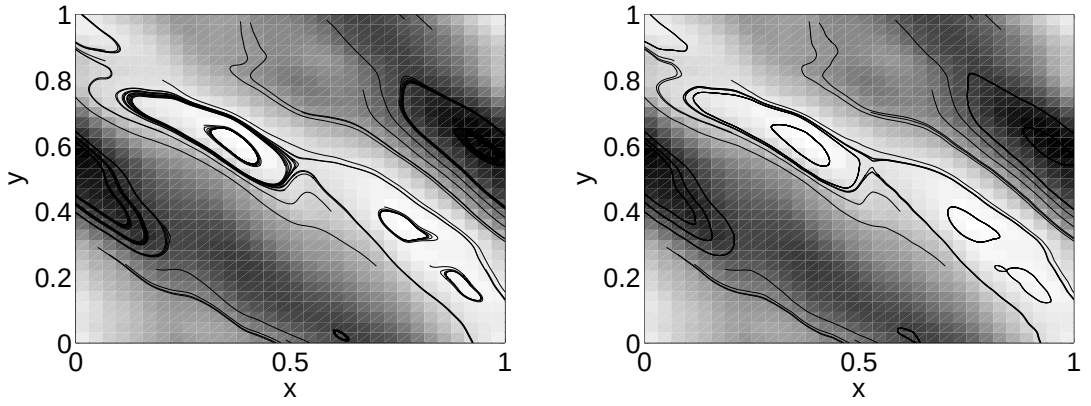

(a) Version 1: interpolation methods applied to $\partial_x \phi$ and $\partial_y \phi$

(b) Version 2: interpolation methods applied to ϕ

Figure 6: Trajectories obtained using polynomial (degree 3) interpolation on grid(s) $\Delta x = \frac{1}{32}$.

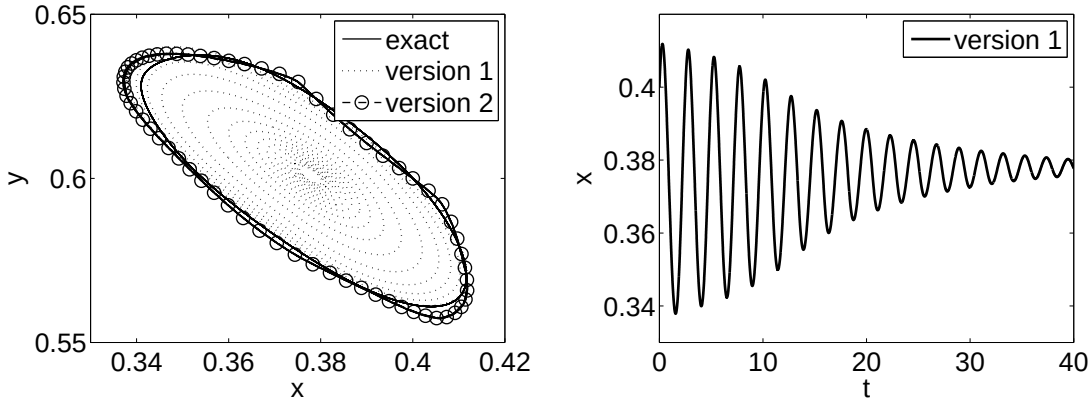

(a)

(b)

Figure 7: Trajectories obtained using PPH subdivision on grid(s) $\Delta x = \frac{1}{32}$.

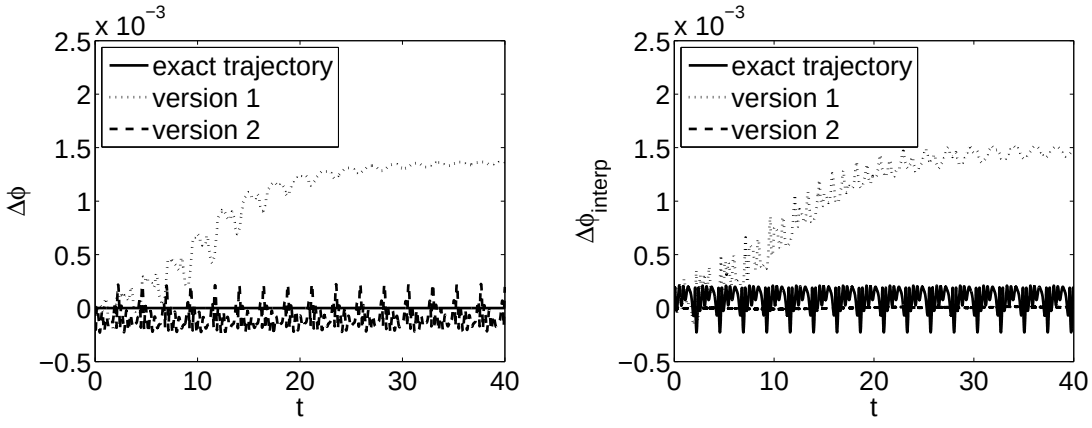

(a)

(b)

Figure 8: Variations of the exact potential and the interpolated potential (PPH) along the trajectoires given in Fig. 7. $\phi(t = 0) \approx 0.0344268$.

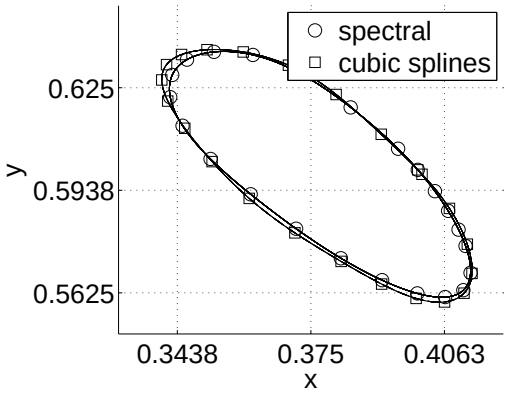

Figure 9: Trajectories obtained using the conservative version for $x_0 = 0.4$, $y_0 = 0.6$, and $\Delta x = \frac{1}{32}$.

conservation of the exact potential ϕ, or the conservation of the interpolated potential ϕ_{interp}. The trajectories obtained using spectral and cubic splines interpolations are shown in Fig. 9, and the corresponding conservation of the potential is shown in Fig. 10. The variations of the interpolated potential are low but show some dissipation due to the numerical integration, and a quasi-periodicity is observed due to the number of complete turns the particle performs in the simulation. Potential variations along the trajectories are found to be weak and periodic. Tab. 3 summarizes the results for the different interpolation methods, the best conservation of the interpolated potential obtained for spectral interpolation and cubic splines can be explained by the regularity of the interpolated potential using these methods, see Tab. 1.

Interpolation	Classical method			Subdivision scheme	
	polynomial degree 3	spectral	cubic splines	Lagrange	PPH
$\max \lvert\Delta\phi\rvert$	2.5991e-004	1.1222e-004	1.3009e-004	2.4252e-004	2.3705e-004
$\max \lvert\Delta\phi_{\text{interp}}\rvert$	1.1517e-005	2.5352e-010	2.4442e-010	3.1077e-006	1.3625e-005

Table 3: Potential conservation along the trajectories obtained using different interpolation methods (conservative version) for $x_0 = 0.4$, $y_0 = 0.6$, and $\Delta x = \frac{1}{32}$.

5.1.3. Lagrangian statistics (averaged errors)

Following Ref. [4] and in order to continue the comparison between the conservative and nonconservative versions, we consider sets of $N_p = 125$ particles with initial positions randomly distributed in $[0,1] \times [0,1]$ (uniform distribution), and compare at each instant the approximated trajectories to the true ones obtained using the analytic expressions of the velocities at each point. The exact trajectories $\mathbf{x}_{\text{exa}}$ are obtained without interpolation using a fourth-order Runge-Kutta scheme with a time step $\Delta t = \frac{1}{6}\frac{1}{2^{10}}$, while the trajectories $\mathbf{x}_{\text{interp}}$ are obtained using a fourth-order Runge-Kutta scheme with $\Delta t = \frac{\Delta x}{6}$. Then, at each time $t \geq 0$, the errors are averaged over all the particles as follows

$$E(t) = \left(\frac{1}{N_p} \left(\sum_{n=1}^{N_p} \left| \mathbf{x}_{\text{interp}}(t) - \mathbf{x}_{\text{exa}}(t) \right|^2 \right) \right)^{1/2}. \tag{40}$$

Fig. 11 shows the results obtained using the PPH scheme, and Tab. 4 summarizes the results for the different interpolation methods.

Errors using the conservative version (version 2) are less important than using the nonconservative version (version 1) for which errors increase with time, indicating that particles stray from their correct trajectories. Thus version 2 is the most suitable for our problem. This meets up with the fact that the second version takes into account the conservative aspect of the problem. The performance of spectral interpolation for a grid $\Delta x = \frac{1}{64}$ (almost zero error) is explained by the form of the potential (31) (with $\omega = 0$ and $N = 25$) considered here: the grid captures all the relevant modes (up to $N = 25$) and spectral interpolation therefore leads to an exact reconstruction.

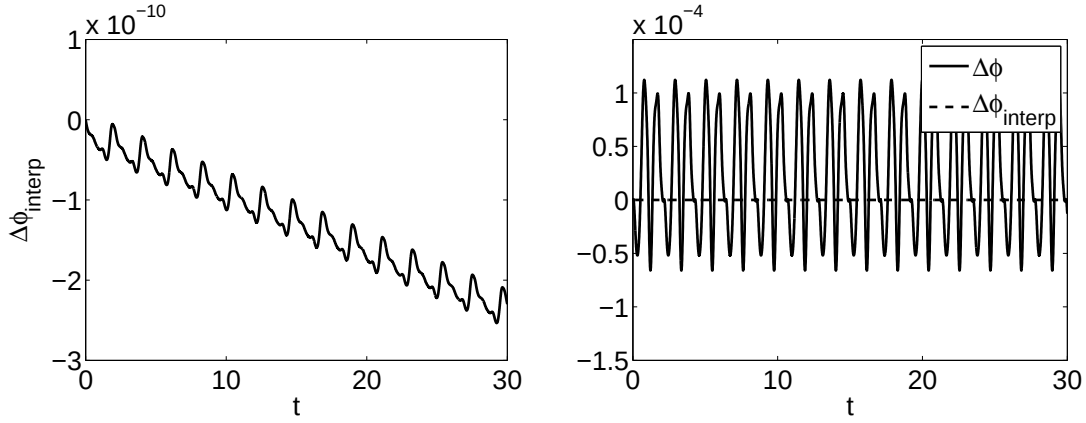

(a) Spectral

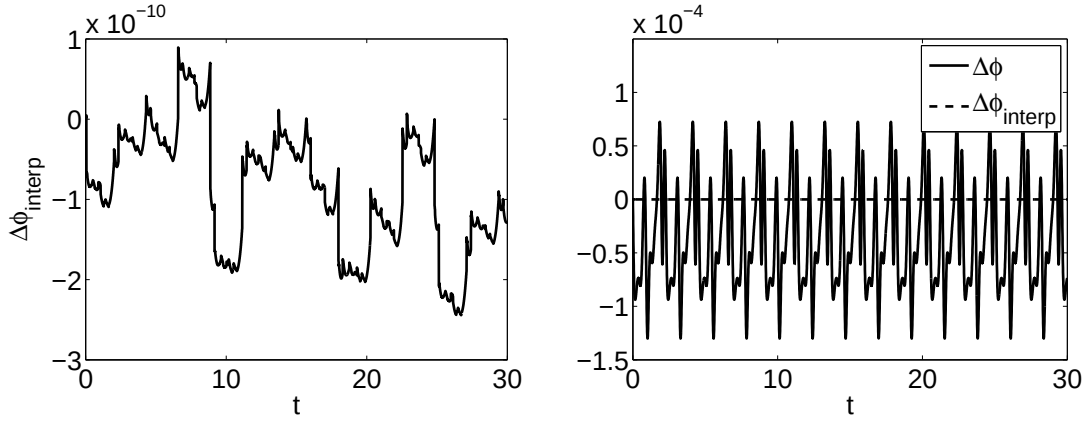

(b) Cubic splines

Figure 10: Variations of the interpolated and the exact potentials along the trajectoires shown in Fig. 9. $\phi(t=0) \approx 0.0344268$.

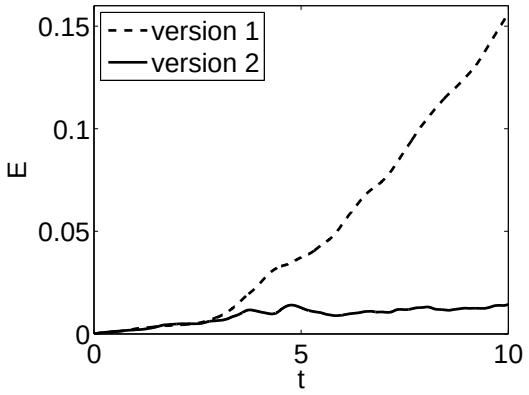

Figure 11: Averaged errors (40) over $N_p = 125$ particles subject to the steady state potential ϕ using PPH subdivision on grid(s) $\Delta x = \frac{1}{64}$.

Interpolation	Classical method			Subdivision scheme	
	polynomial degree 3	spectral	cubic splines	Lagrange	PPH
$\Delta x = \frac{1}{16}$	max E				
Conservative	0.3237	0.3202	0.3099	0.3340	0.3297
Nonconservative	0.5675	0.7092	0.6149	0.5468	0.6708
$\Delta x = \frac{1}{32}$	max E				
Conservative	0.2489	0.2372	0.2495	0.2458	0.2349
Nonconservative	0.2578	0.2694	0.2663	0.2575	0.3275
$\Delta x = \frac{1}{64}$	max E				
Conservative	0.0110	2.5540e-008	0.0043	0.0105	0.0143
Nonconservative	0.0849	9.5695e-012	0.0108	0.0915	0.1563

Table 4: Averaged errors (40) over $N_p = 125$ particles subject to the steady state potential ϕ, obtained using different interpolation methods.

5.2. Nonsmooth potential

We consider again a steady state potential but the potential ϕ is now supposed to be strongly varying. It is of the form:

$$\phi(x, y) = (4y - 2)^2/2 + f(x), \tag{41}$$

where f is a continuous piecewise linear function represented in Fig. 12(b). The potential is illustrated in Fig. 12(a).

As shown in the figures, there are essentially two families of trajectories living either on the left of $x = 0.5$ or on the right of $x = 0.5$.

These two families are separated by a particular point corresponding to a local maximum in the x direction for $y = 0.5$.

As previously, we consider that the potential is only known on a discrete grid. Interpolation is used to reconstruct the potential entirely in order to compare it to the real potential.

Let us focus first on the interpolated points in the x direction: while the PPH scheme reconstructs exactly the sections in this direction, the polynomial interpolation gives rise to a bump (quite similar to the oscillation encountered in the univariate case because of the Gibbs phenomenon) that shifts the local maximum that was mentioned earlier to the right. We remind that this local maximum separates two different regions in the phase space, this means that using polynomial interpolation, a particle that normally belongs to the family of the right side, will belong to the family of left side. This is exactly what is shown on Fig. 13.

5.3. Time dependent potential

We return to the general case of a time dependent potential $\phi(x, y, t)$ and the corresponding equations of motion given by Eq. (30). In this case, the potential is no longer conserved along the trajectory. Indeed $\frac{d\phi}{dt} = \partial_x\phi\,\dot{x} + \partial_y\phi\,\dot{y} + \partial_t\phi = \partial_t\phi \neq 0$. However by introducing a new variable E which evolves according to $\dot{E} = -\partial_t\phi(x, y, t)$,

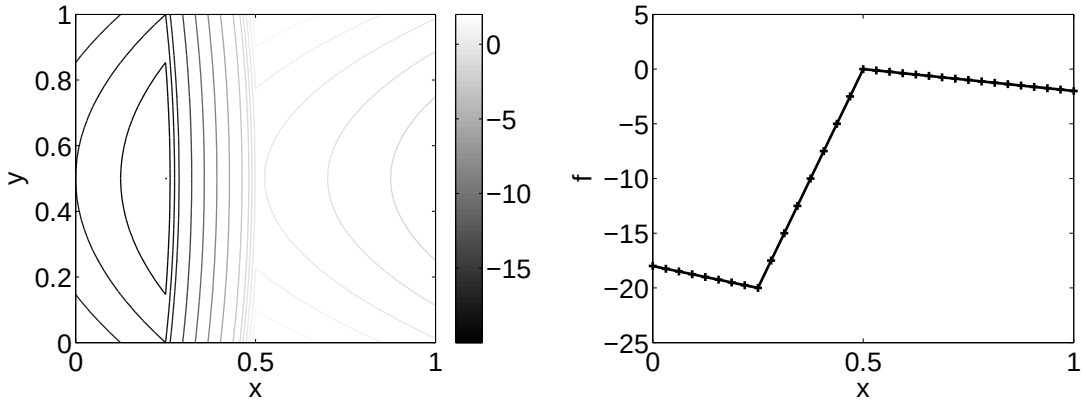

(a) Contour plot

(b) Function f corresponding to $\phi(\cdot, 0.5)$

Figure 12: Nonsmooth potential given by Eq. (41).

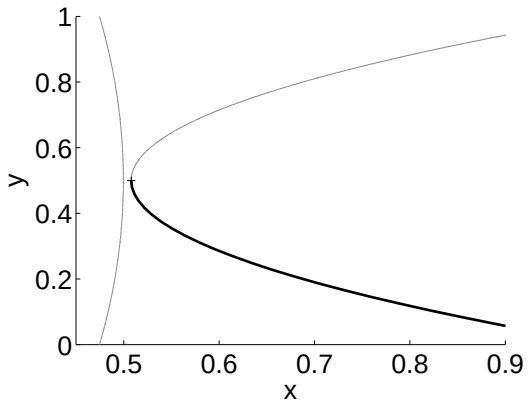

(a) Exact

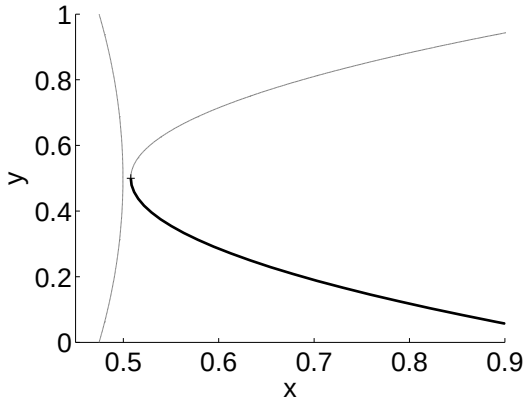

(b) PPH scheme

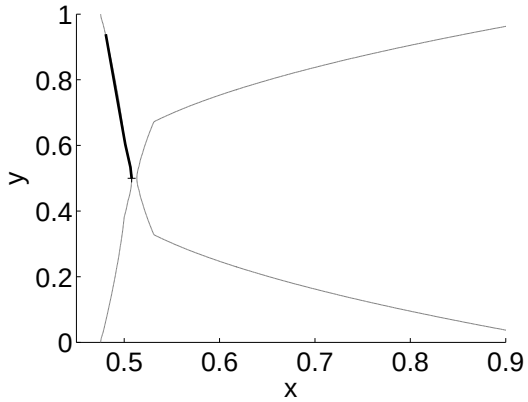

(c) Polynomial interpolation degree 3

Figure 13: Isovalues (thin line) and trajectories (thick line) obtained for a particle initially placed at the same position $(x_0, y_0) = (0.5 + \frac{1}{2^7}, 0.5)$ and subject to the nonsmooth potential (41).

we restore the Hamiltonian structure. The autonomous Hamiltonian of the model is $H = E + \phi$ and $\frac{dH}{dt} = 0$ along the trajectory. Again given the conservative aspect of the problem, in the sequel we adopt the conservative interpolation version (version 2). The conservative approach when ϕ is only known on a grid consists in considering the following system

$$\begin{cases} \dot{x} = -\partial_y \phi_{\text{interp}}(x, y, t), \\ \dot{y} = \partial_x \phi_{\text{interp}}(x, y, t), \\ \dot{E} = -\partial_t \phi_{\text{interp}}(x, y, t). \end{cases}$$

Note that the evaluation of E is only required if the conservation of $E + \phi_{\text{interp}}$ must be checked.

5.3.1. More "realistic" potential

To test the interpolation scheme on a realistic time-dependent potential, $\phi(x, y, t)$, we consider the electrostatic potential fields encountered in the edge turbulence of magnetically confined fusion plasmas. Turbulent transport determines the confinement of high temperature plasmas encountered in these fusion devices, and hence is of interest with regards to the efficiency of energy extraction.

Among the phenomena observed at the outer edge of fusion plasmas, we are interested in the trajectories of charged impurities produced by the interaction of the plasma with the main chamber, impurities that are carried by the turbulent velocity field according to

$$\begin{pmatrix} \dot{x} \\ \dot{y} \end{pmatrix} = \begin{pmatrix} -\partial_y \phi(x, y, t) \\ \partial_x \phi(x, y, t) \end{pmatrix}. \tag{42}$$

Because of their very low concentration, these charged impurities do not modify the plasma electric potential ϕ, and consequently they are considered as passive scalars. However depending on their spreading in the plasma domain, they can deteriorate significantly the plasma confinement and stability and therefore the performance of the device. For these reasons it is important to understand as much as possible their dynamics [23, 24, 25, 26, 27].

The turbulent electric field from which they are advected is obtained from the following 2D fluid equations [28, 29]:

$$\begin{aligned} \left\{ \frac{\partial}{\partial t} + [\phi, \cdot] - D_n \nabla^2 \right\} n &= -\sigma n e^{\Lambda - \phi} + S_o(x), \\ \left\{ \frac{\partial}{\partial t} + [\phi, \cdot] - \nu \nabla^2 \right\} \Omega &= \sigma n \left(1 - e^{\Lambda - \phi}\right) - g \frac{\partial n}{\partial y}. \end{aligned} \tag{43}$$

These equations for plasma density n and vorticity $\Omega = \nabla \cdot (n \nabla \phi)$ model plasma electrostatic turbulence in the section transversal to the magnetic field in the peripheral region of the tokamak, the toroidal device where the plasma is magnetically confined. The study of electrostatic turbulence can be reduced to a 2D problem using the so called flute approximation, based on the fact that the fluctuations in the direction parallel to the magnetic field are much smaller than those in the perpendicular direction. In this case the computational domain, considered in a Cartesian geometry, is composed of a radial direction x and a poloidal one y. The radial direction is normalized such that $x = (r - a)/\rho_s$ with a the plasma minus radius, r the radius of the considered magnetic surface and ρ_s the hybrid Larmor radius. The poloidal direction $y = a\theta/\rho_s$ represents the poloidal angle on the magnetic surface, with θ the actual poloidal angle.

The first equation is obtained from the balance equation for plasma electron density n and the second one from charge conservation in the quasi neutral limit. More precisely, in the plasma density equation, one considers the advection term due to the electric drift velocity, expressed by the Poisson bracket $[\phi, n] = (\partial_x \phi \partial_y n - \partial_y \phi \partial_x n)$ and a small diffusion smoothing term with coefficient D_n. On the right hand side one has a density source term S_o, that is localized spatially at the entrance of the domain and that represents the source of density due to the plasma of the central region and that maintains the system out of the thermodynamic equilibrium.

The sink term is given by $-\sigma n e^{\Lambda - \phi}$ where σ is a control parameter proportional to the saturation current and where Λ is the plasma potential with respect to the reference potential of the wall. Indeed this term takes into account the losses of plasma density produced by the interaction of the plasma with solid components. In this outer region of the tokamak, called Scrape Off Layer, the plasma is in contact with solid objects, like the especially designed facing components for the extraction of particles called divertor or limiters. The interaction between the plasma and the solid objects results in the recombination of the charged plasma particles, that is translated with an appropriate loss term in the fluid equations (see [28]).

Concerning the vorticity equation, on the left hand side one has the same structure of the density equation with the advection term due to the $\mathbf{E} \times \mathbf{B}$ drift velocity and a relatively small viscosity term proportional to the

coefficient ν. On the right hand side the loss term has a particular structure given by the physics of the SOL and governs the damping of the large scale structures. The g term is the driving turbulence term and is associated with the curvature drift and the separation of charges. It has been simplified to a coupling to the poloidal density gradient. It is equivalent to the gravity term when addressing buoyancy effects in a neutral fluid.

Numerically, we obtain the time and space dependent density and potential fields from computations performed using the spectral code *TOKAM-2D* [28] in which Eqs. (43) are evolved in time using a second-order predictor-corrector scheme. Spatial derivatives are computed in TOKAM-2D using spectral schemes, thereby providing a reference case for comparing the results of various interpolation schemes.

In the following sections, we consider two physical situations for charged test particle simulations. First we consider the behaviour of charged test particles advected by the electric potential and initially located in one of the coherent structures that appear in the density field. A comparison of their dynamics with the one of the structures is performed. Then we analyze the influence of an external biasing of a probe on the potential field and the dynamics of test particles initially located in this biased region.

5.3.2. Propagation of structures

Here we consider the density and potential fields obtained from TOKAM-2D flux driven simulations as introduced in the previous section. In Fig. 14 is represented the normalized density field at four different time steps. The normalized density field that we indicate with $C(x, y, t)$ is obtained as follows

$$C(x, y, t) = n(x, y, t)/\langle n(x, y, t)\rangle_{y,t}. \tag{44}$$

This normalization takes into account the strong radial decay of density due to the sink term and allows one to have a better visualization of the regions in the far SOL (large radial coordinate). We remark the ballistic propagation of overdense structures from the source to the far SOL as well as the ballistic propagation of subdense structures in the opposite direction. We do not aim here to compare different interpolation methods, but rather to use test particle simulations [30] in order to understand the link between the propagation of coherent structures in the density field and the spreading of test particles initially located within the structure. Considering the sharp variations of the potential at the location of the structures, accuracy of interpolation determines our ability to successfully trace the trajectory of a particle on the structure.

Given the results obtained in the previous sections, we use the PPH scheme performing interpolation in space on the potential field generated by TOKAM-2D and given on a grid $N_x \times N_y = 256 \times 256$ (the domain is periodic in both spatial directions) at each time step ($\Delta t = 1$). The time integration is performed using a second-order Runge-Kutta scheme as for the fluid equations of TOKAM-2D. Working with the turbulent field represented in Fig. 14, we consider 208 test particles initially inside a density structure and follow their evolution in time comparing their position to the evolution of the structure in the density field. The initial configuration is given in Fig. 14(a). After some time we notice that the particles catch up the forefront of the structure (Fig. 14(b)) which means that the radial velocity of particles is larger than the one of the structure. Next, particles are pushed behind (Fig. 14(c)), then spread around (Fig. 14(d)) and finally are trapped by other structures.

This shows that density structures are not made with the same particles when they evolve: there is a difference between the individual trajectories of particles and the global propagation of structures. The mechanism of convection is similar to a vortex dipole. The streamlined picture of the dipole shows that particles keep circulating from the front to the back of the structure. What we see is that when there is radial asymmetry this circulation is broken. Particles go from center to front, then from front to back; in an idealized case of an isolated structure they should return to front, but some of the particles fail to complete the full loop. The radial asymmetry in the vorticity in these structures leads to the formation of steep fronts at the head and extended tails at the rear end of the structure [31]. In the presence of surrounding structures, we thus see a loss of particles in the tail to other structures.

We focus our study on the density structure initially located in the region around $(x, y) = (80, 150)$ and identified by the contour value $C^* = 1.22$. The structure is represented with a black contour in Fig. 14. We consider an ensemble of 208 particles with initial conditions within this structure, that is for all particles, $C_i > C^*$. As time progresses, fewer and fewer particles remain at a level C greater than C^*, that is fewer and fewer particles remain trapped. In Fig. 15 is shown the number of trapped particles versus time: during a time $\delta t \approx 716\Omega_i^{-1}$, that we call *coherence time*, all particles evolve remaining inside the structure. After this coherence time a lot of particles escape from the structure on a relatively short time producing a first strong decay in the number of trapped particles. A third phase with an escaping time much smaller than the first one is observed before the final time considered in Fig. 14, when only 18.27% of these particles are still trapped in their original density structure.

According to the observed evolution of the particles and the structure, a difference between the radial velocity of particles and the radial velocity of the structure is expected.

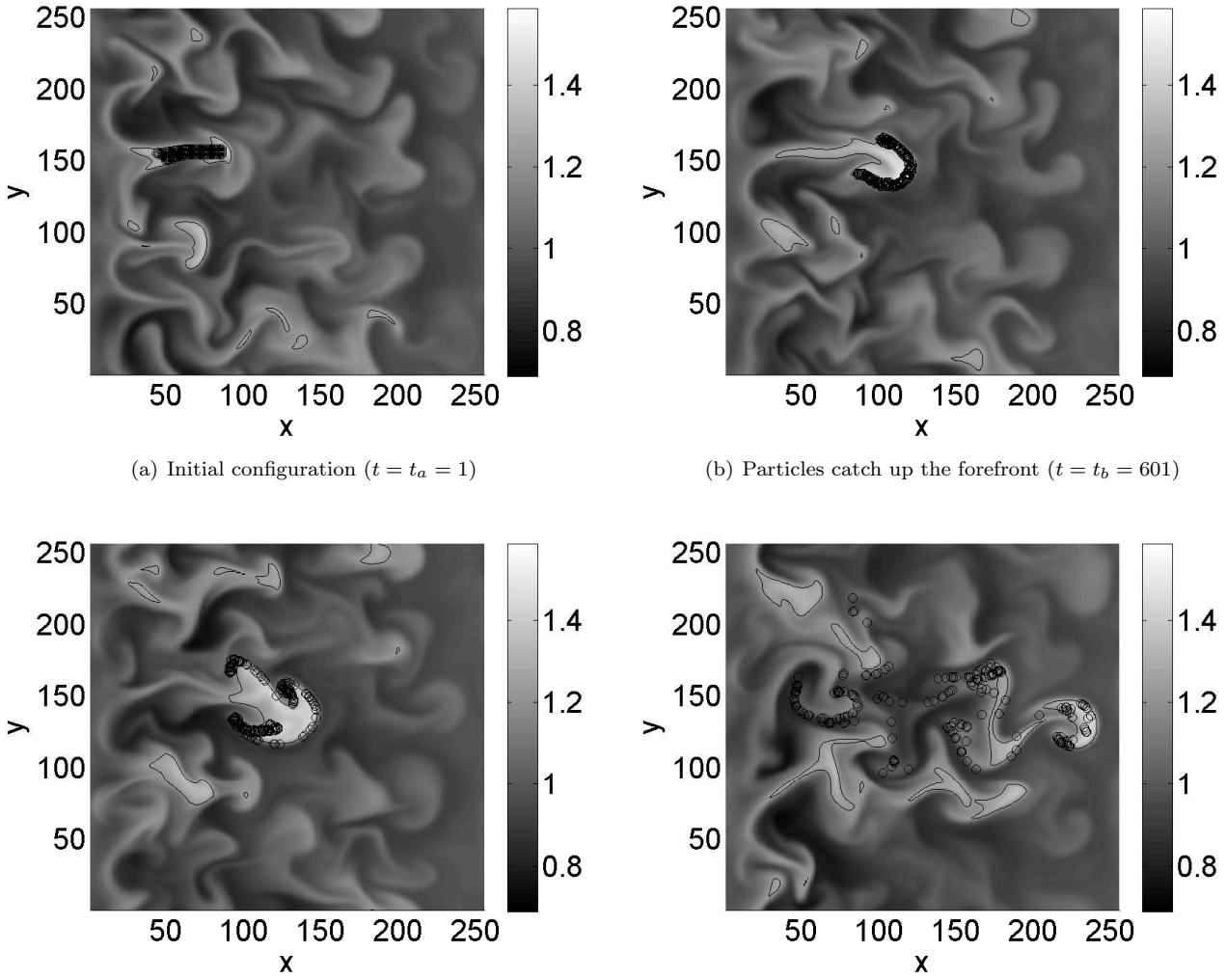

(a) Initial configuration ($t = t_a = 1$)

(b) Particles catch up the forefront ($t = t_b = 601$)

(c) Particles are pushed behind ($t = t_c = 1201$)

(d) Particles spread around ($t = t_d = 3301$)

Figure 14: Propagation of particles and structures in the turbulent case.

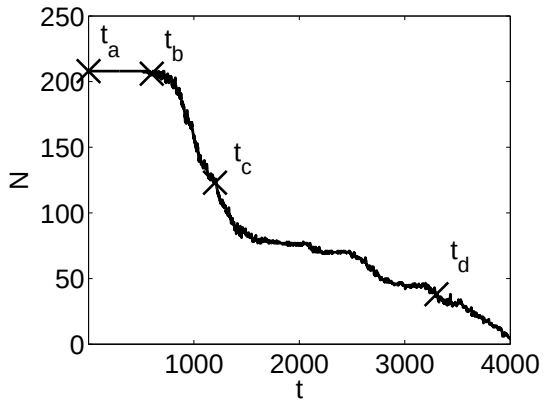

Figure 15: Number of trapped particles in the structure versus time. The crosses correspond to the times (t_a, t_b, t_c, t_d) considered in Fig. 14.

For illustration, it is expected that the particle initially located at the tail of the structure reaches the head of the structure in a time equal to the coherence time, which means roughly $V_p \delta t \approx \Delta_s + V_s \delta t$, where V_p and V_s are respectively the average velocity of the particle and the average velocity of the structure during the coherence time δt, and Δ_s stands for the radial extent of the structure. This expression can be rewritten as

$$V_p - V_s \approx \frac{\Delta_s}{\delta t}. \tag{45}$$

A schematic representation of this idea is given in Fig 16. In the following we check the validity of this picture using the simulation results. One has to give an estimation of the radial size of the $2D$-structure, of its radial velocity V_s and the radial velocity V_p of the considered particle.

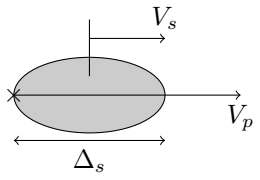

Figure 16: Schematic representation of a density structure of size Δ_s moving with velocity V_s, and of a particle located at the tail of the structure moving with velocity V_p.

The estimation of the radial size of the structure Δ_s is obtained in the following way: we compute the center of mass of the structure in the (x, y) plane as $(x_g, y_g) = (\sum_j x_j C_j / \sum_j C_j, \sum_j y_j C_j / \sum_j C_j)$ where the sums are taken over all grid points contained in the structure under consideration. The radial extent of the structure is then obtained computing the difference between the maximum and the minimum of the radial coordinates of the structure grid points with $y_i = y_g$. This procedure gives a relatively good estimation if applied during the coherence time when the structure is not distorted too much in the poloidal direction.

Taking the mean value of these estimations over coherence time one obtains $\Delta_s \approx 46.5 \rho_s$. Since the coherence time has been initially evaluated as $\delta t \approx 716 \Omega_i^{-1}$, one has $\frac{\Delta_s}{\delta t} \approx 0.0649\ c_s$. This value should correspond to the difference between the particle velocity V_p and the structure velocity V_s, that are estimated as follows. The velocity of the structure V_s is given by the displacement of its center of mass between $t = 1$ and $t = 1 + \delta t$, we find $V_s \approx 0.0528\ c_s$. The velocity of the particle is also obtained by its displacement during the coherence time. We find $V_p \approx 0.1111\ c_s$ for the particle located in the queue of the structure (with the smallest radial coordinate at initial time). One obtains $V_p - V_s \approx 0.0583\ c_s$, consistent with the first estimate of $\frac{\Delta_s}{\delta t}$.

Starting from this one dimensional analysis now we look at the influence of the poloidal motion on the spreading of particles. As a first observation we show in Fig. 17 the trajectories of 5 particles with the same radial coordinate but different poloidal positions at the initial time.

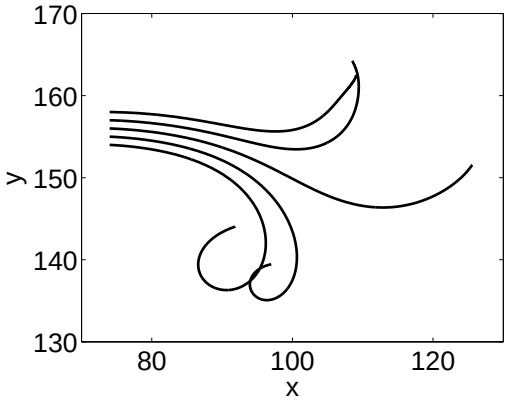

Figure 17: Trajectories of 5 particles with the same value of the initial x-coordinate during the coherence time.

We remark that the particle at the center of the structure is essentially accelerated radially while those located toward the edge are also advected in the poloidal direction. An estimation of this effect can be obtained considering as previously the difference between the radial velocity of the particles and the radial velocity of the structure.

However this time we consider the mean value $\langle V_p \rangle_\Delta$ obtained averaging the radial velocity over all particles having as initial condition the same radial coordinate but with different poloidal positions, as schematically represented in Fig 18. The equation becomes

$$\langle V_p \rangle_\Delta - V_s \approx \frac{\Delta}{\delta t}, \tag{46}$$

where Δ is the initial distance of particles to the head of the structure.

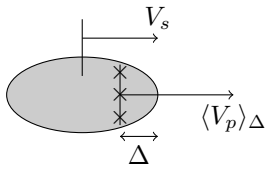

Figure 18: Schematic representation of a density structure and of the particles located at a distance Δ from the head of the structure.

The results are shown in Fig. 19 where the two quantities $\langle V_p \rangle_\Delta - V_s$ and $\frac{\Delta}{\delta t}$ are represented as functions of the radial position. We observe that the difference between the expected value and the measured one varies as a function of the initial radial position. More precisely the difference between these two quantities is of order 10^{-2} for the particles initially placed far from the head of the structure, and increases as Δ decreases, that is for particles initially closer and closer to the head. The particles initially located at the tail of the structure are essentially accelerated in the radial direction and the poloidal motion is relatively small. On the contrary, for particles closer to the head, the poloidal advection starts from the beginning resulting in a reduced radial velocity.

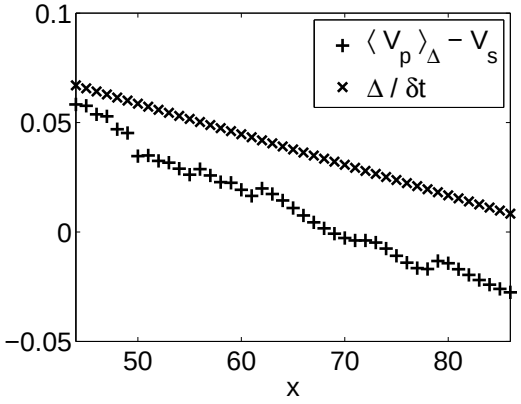

Figure 19: Plots of $\langle V_p \rangle_\Delta - V_s$ and $\frac{\Delta}{\delta t}$ versus x.

In Fig. 20(a) we show the instantaneous velocities of some particles during the coherence time and the average of the velocities of all particles during this same time. One remarks essentially three phases in the motion of particles. A first phase, when the radial acceleration is dominant for almost each particle composing the structure, a second one during which a lot of particles start to have an important poloidal advection and consequently a strong reduction of their radial velocity. Finally a third phase when the structure itself is strongly deformed poloidally and the particles experience a redistribution in the poloidal direction with almost null or negative radial velocity.

Moreover we observe that the individual velocities are spread around the mean velocity, the standard deviation $\sigma_V = \sqrt{\langle (V_p - \langle V_p \rangle)^2 \rangle}$ versus time is given in Fig. 20(b).

The sketch that emerges from this analysis is that during the evolution of a coherent structure there is a continuous exchange of particles with the surrounding plasma. Particles initially located into the structure tend to move towards the forefront of the structure, then their radial trajectories become poloidal and finally are advected by other structures. On the other hand, one expects that particles initially located outside the structure will be captured during their evolution. We do not address in this paper the question of where do the particles that replace the escaping ones come from, even if a first idea can be given by looking at the velocity field in the vicinity of the structure under consideration.

The velocity field plotted in Fig. 21 at two different times shows that the radial velocity is important inside the structure but decreases at the head of the structure, which explains the fact that the particles do not exceed

the structure despite the fact that they are going faster. Moreover one observes that around the structure there are *exchange zones* characterized by a velocity field carrying particles into the structure and other regions where the velocity field is almost null that are decoupled from the structure by the presence of a sort of barrier to the exchange of particles.

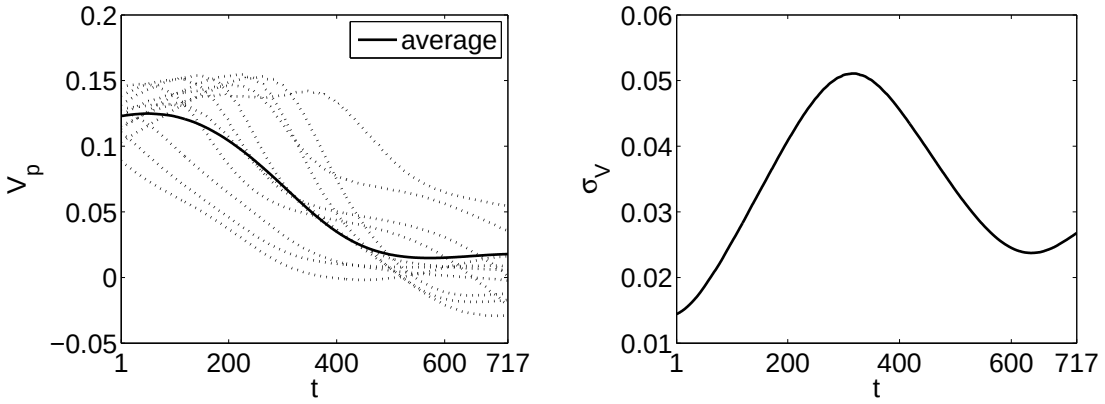

(a) (b)

Figure 20: (a): Instantaneous velocities in the x-direction of 11 particles during the coherence time (dotted line) and average of the velocities of the 208 particles (solid line). (b): Measure of dispersion by standrad deviation versus time.

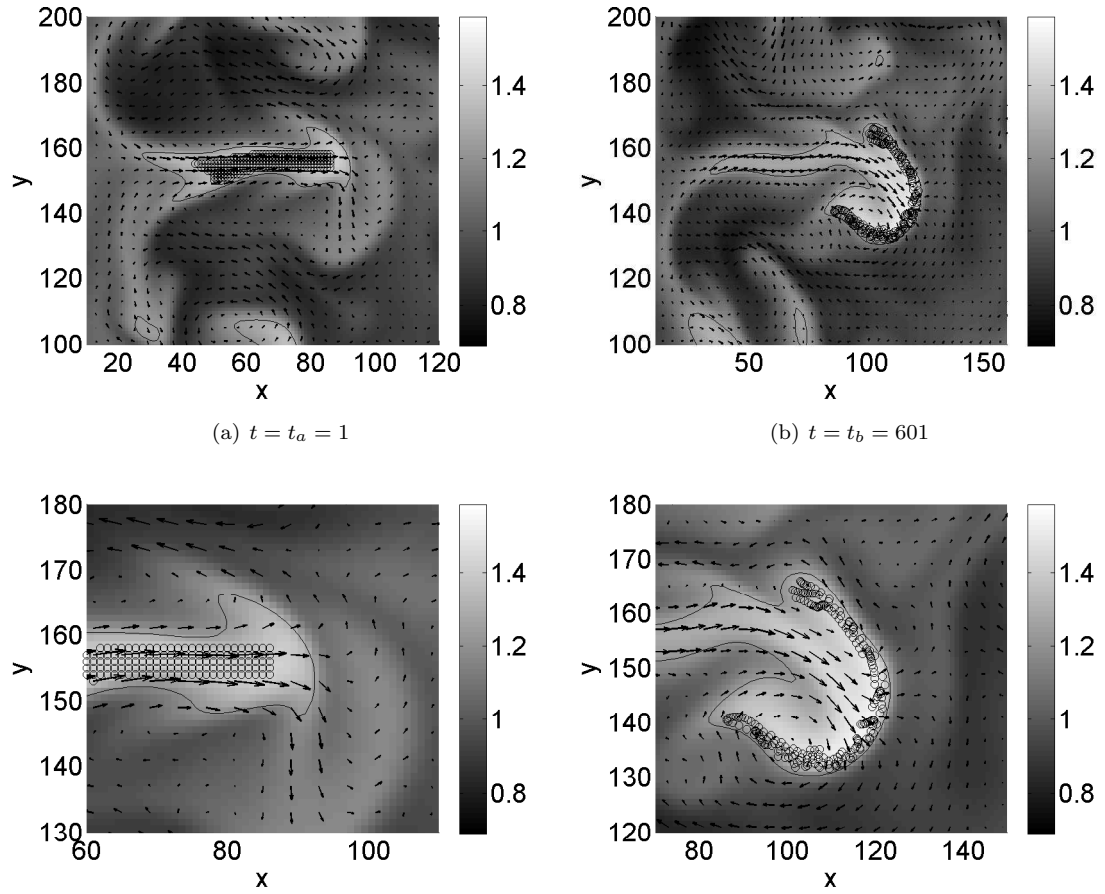

(a) $t = t_a = 1$ (b) $t = t_b = 601$

(c) $t = t_a = 1$ (d) $t = t_b = 601$

Figure 21: Density and velocity field near the structure under consideration.

5.3.3. Influence of a probe

We consider potential and density fields generated by TOKAM-2D in the presence of a probe [29]. The fields $N_x \times N_y = 512 \times 256$ are represented in Fig. 22 where one can see the footprint of the probe. Particles inside the probe are expected to stay there as shown by the velocity field represented in Fig. 22(c). Fig. 22(d) shows a section of the potential in the y-direction that crosses the location of the probe, one sees that the applied potential is 4 times the typical fluctuation and rather smooth.

Here, the region of trapped particles is determined by the contour of the probe, which corresponds to a local maximum near the probe in the cross-section. In that sense, this part follows the previous part dealing with a nonsmooth potential: describing correctly the behaviour of a particle in the probe depends strongly on the good reconstruction of the potential using a given interpolation method. It is above all crucial to reproduce finely the contour (local maximum) separating different regions in the phase space.

To compare the interpolation methods in this context, we have randomly selected 100 particles in the probe region at different levels of the potential 'well', as shown in Fig. 23(a). We compute the trajectories using three-dimensional versions of the interpolation methods coupled with a second-order Runge-Kutta time integration scheme as in TOKAM-2D with $\Delta t = 1$, over a discretized potential $256_x \times 128_y$ given every 50 time steps. The results give 75% of trapped particles using the PPH scheme against 71% of trapped particles with the polynomial interpolation (due to the non-periodicity in the time direction, we limited ourselves to local interpolation methods and integration is performed from $t_0 = 501$ to $t_f = 14501$). The number of trapped particles versus time is shown in Fig. 24 (we considered that the contour of the probe is the circle represented in Fig. 23(a)), the small difference observed between PPH subdivision and polynomial interpolation can be explained by the relative smoothness of the fields considered here.

The reader might expect the particle confinement rate to be 100%, but since it is a turbulent field with a dependence on time, the large fluctuations in the potential influence the particles located near the edge of the probe, which could then get out of the probe (whose contour is itself varying in time), and thus the confined particles are going to be below that level.

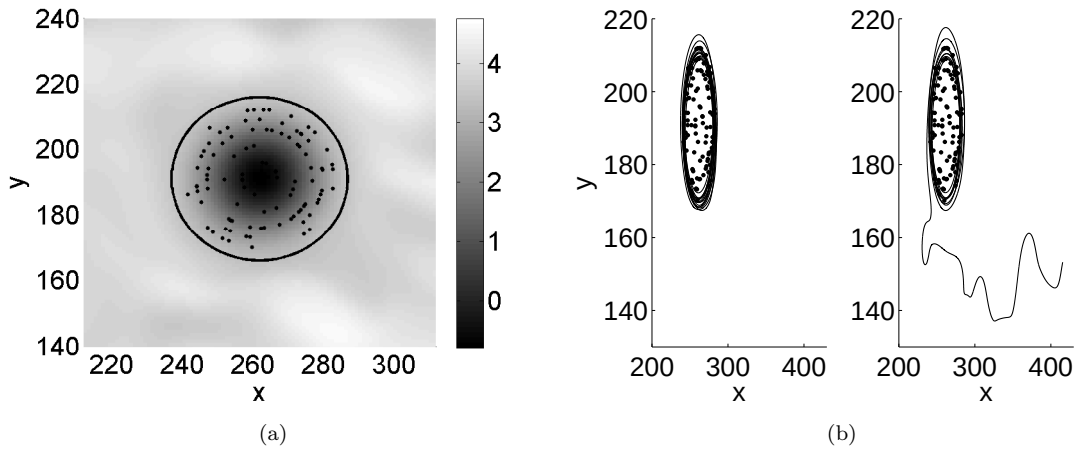

(a) (b)

Figure 23: (a): Contour plot of the potential field in the probe region and initial conditions for test particles inside the probe (black dots), the circle is a representation of the edge of the probe. (b): Comparison between trajectories using PPH scheme (left) and polynomial interpolation (right) starting from the same initial condition.

For particles that are inside the probe far enough from its contour, we find that they are trapped regardless of the interpolation method used, but as the distance to the center increases (see the particles near the boundary of the probe region in Fig. 23(a)), some particles can escape. An example of the different particle dynamics obtained depending on the interpolation scheme used is shown in Fig. 23(b) where starting from the same initial condition (chosen near the probe boundary), a particle remains trapped in the probe region using PPH scheme and escapes using polynomial interpolation.

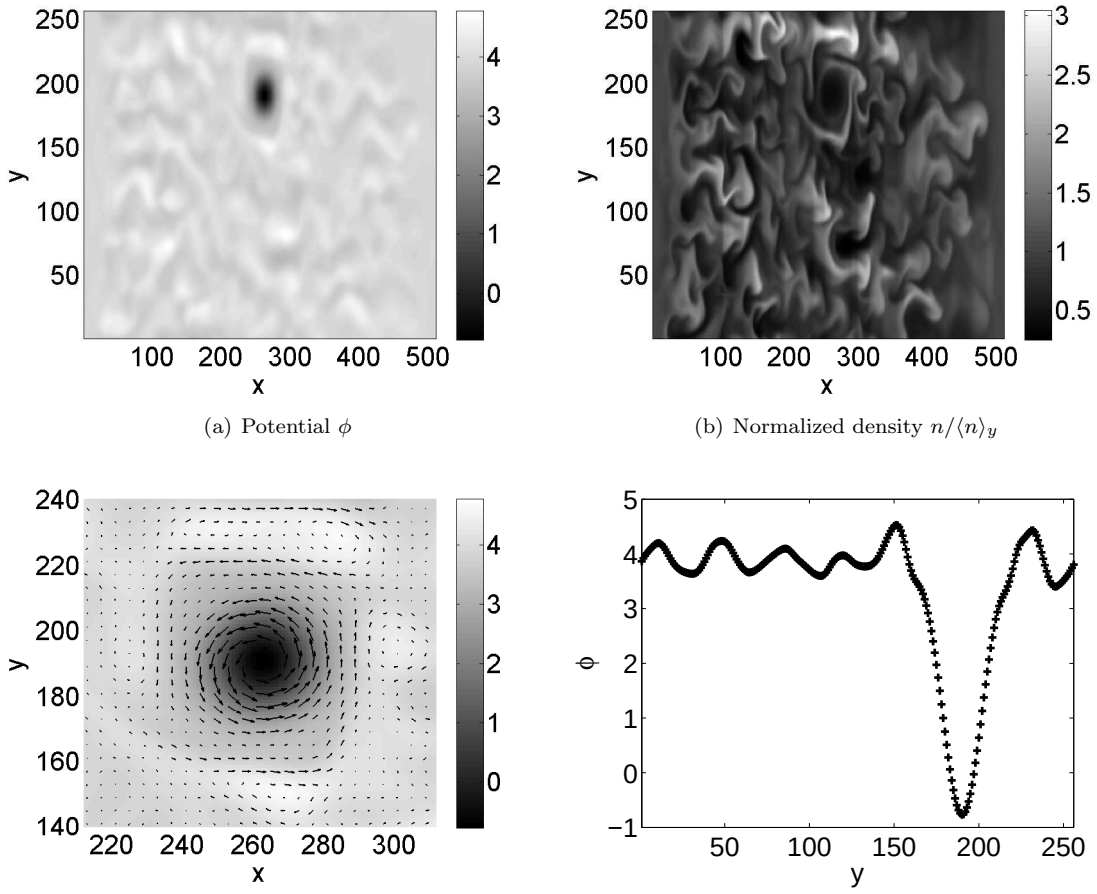

(a) Potential ϕ

(b) Normalized density $n/\langle n\rangle_y$

(c) Potential ϕ and velocity field near the probe

(d) Potential section in the y-direction at $x = 262$

Figure 22: Potential and density fields generated by TOKAM-2D in the presence of a probe centered at $x = 262$, $y = 190$. Note that $\langle n\rangle_y$ is a function of x and t.

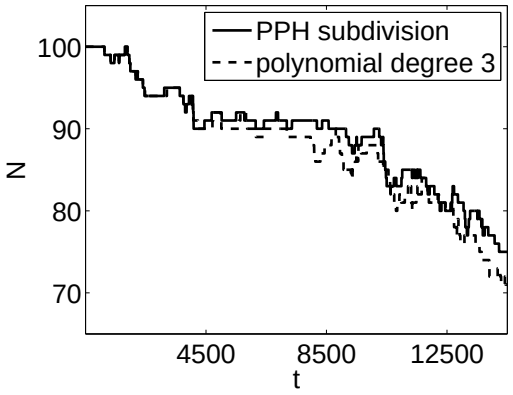

Figure 24: Number of trapped particles in the probe versus time.

6. Conclusion

The simulation of the propagation of particles in a discrete velocity field drastically relies on interpolation operators as shown by the theoretical and numerical results of this paper. Such a situation of discrete velocity field is often found if the field is the result of a numerical code or an experimental measurement. The situation may be all the more drastic as the field has discontinuities or at least strong gradients. In that framework, it has been shown that nonlinear subdivision schemes can advantageously be substituted to classical linear operators. This advantage has been highlighted first on a critical 1D velocity field with a discontinuity leading to the Gibbs phenomenon when classical linear interpolation methods are used, and then on a 2D velocity field deriving from a nonsmooth potential where the separation of different regions in the phase space may not be recovered with accuracy using classical methods. In these two situations, particles can be deflected from their correct trajectories if one uses classical methods.

The proposed interpolation operator for tracking based on the nonlinear Piecewise Parabolic Harmonic (PPH) subdivision scheme was applied in a realistic case of turbulent time-dependent potential fields related to magnetically confined plasmas. The method has been used to study the propagation of coherent structures and we also investigated the case of a potential in the presence of a probe for its similarity to the 2D nonsmooth potential case by the presence of 2 different regions: the inside and the outside of the probe.

From a physical point of view, the propagation of structures through plasma was compared to the propagation of the particles composing them, this comparison showed a significant difference suggesting that there is a transfer of particles between the density structures and the surrounding plasma. This difference between the overall structures spread and the propagation of the constituent particles can be found in more generic situations such as the traffic of vehicles in highways.

Attention has been given in the foregoing to use a conservative interpolation version when dealing with a velocity deriving from a potential (stream function), in order to keep the Hamiltonian structure of the problem: it consists in interpolating the discrete potential and then differentiating the interpolated potential. A Quantitative comparison was made between conservative and nonconservative versions on an analytical test potential.

Acknowledgements

This work was supported by the European Community under the contract of Association between EURATOM, CEA, and the French Research Federation for fusion study. The views and opinions expressed herein do not necessarily reflect those of the European Commission. This work was financially supported by the ESPOIR project, ANR-09-BLAN-0035-01, http://sites.google.com/site/anrespoir/.

References

[1] P. K. Yeung, S. B. Pope, An Algorithm for Tracking Fluid Particles in Numerical Simulations of Homogeneous Turbulence, J. Comput. Phys. 79 (1988) 373–416.

[2] S. Balachandar, M. R. Maxey, Methods for Evaluating Fluid Velocities in Spectral Simulations of Turbulence, J. Comput. Phys. 83 (1989) 96–125.

[3] H. Homann, J. Dreher, R. Grauer, Impact of the floating-point precision and interpolation scheme on the results of DNS of turbulence by pseudo-spectral codes, Comput. Phys. Commun. 177 (2007) 560–565.

[4] A. L. Rovelstad, R. A. Handler, P. S. Bernard, The Effect of Interpolation Errors on the Lagrangian Analysis of Simulated Turbulent Channel Flow, J. Comput. Phys. 110 (1994) 190–195.

[5] L. Biferale, G. Boffetta, A. Celani, A. Lanotte, F. Toschi, Particle trapping in three-dimensional fully developed turbulence, Phys. Fluids 17 (2005) 021701.

[6] B. L. Sawford, P. K. Yeung, Eulerian acceleration statistics as a discriminator between Lagrangian stochastic models in uniform shear flow, Phys. Fluids 12 (2000) 2033.

[7] A. L. Porta, G. A. Voth, A. M. Crawford, J. Alexander, E. Bodenschatz, Fluid particle accelerations in fully developed turbulence, Letters to Nature 409 (2001) 1017–1019.

[8] H. Homann, R. Grauer, A. Busse, W. C. MÃ$\frac{1}{4}$ller, Lagrangian Statistics of Navier-Stokes- and MHD-Turbulence, J. Plasma Physics 73 (2007) 821–830.

[9] W. J. T. Bos, B. Kadoch, S. Neffaa, K. Schneider, Lagrangian dynamics of drift-wave turbulence, Physica D 239 (2010) 1269–1277.

[10] S. Amat, A review on the piecewise polynomial harmonic interpolation, Appl. Numer. Math. 58 (2008) 1168–1185.

[11] J. P. Boyd, Chebyshev and Fourier Spectral Methods, Dover Publications, 2001.

[12] C. K. Chui, An Introduction to Wavelets, San Diego, Academic Press, 1992.

[13] V. Perrier, C. Basdevant, La dÃ©composition en ondelettes pÃ©riodiques, un outil pour l'analyse de champs inhomogÃ¨nes. ThÃ©ories et algorithmes., Rech. AÃ©rosp. 3 (1989) 53–67.

[14] N. Dyn, Subdivision Schemes in Computer-Aided Geometric Design, Computer Aided Geometric Design 20 (4) (1992) 36–104.

[15] S. Amat, J. Liandrat, On the stability of the PPH nonlinear multiresolution, Appl. Comp. Harm. Anal. 18 (2005) 198–206.

[16] M. Crouzeix, A. L. Mignot, Analyse numérique des équations différentielles, Masson, 1984.

[17] C. Lobry, T. Sari, Équations diffÃ©rentielles Ã second membre discontinu, in: ContrÃ´le non linÃ©aire et Applications, 2005.

[18] A. F. Filippov, Differential Equations with Discontinuous Righthand Sides, Kluwer Academic Publishers, 1988.

[19] G. Ciraolo, F. Briolle, C. Chandre, E. Floriani, R. Lima, M. Vittot, M. Pettini, C. Figarella, P. Ghendrih, Control of Hamiltonian chaos as a possible tool to control anomalous transport in fusion plasmas, Phys. Rev. E 69 (2004) 056213.

[20] R. J. Goldston, P. H. Rutherford, Introduction to plasma physics, Plasma Physics Series, Institute of Physics Pub., 1995.

[21] L. D. Landau, E. M. Lifshitz, L. Claude, MÃ©canique, Physique ThÃ©orique, Mir, 1988.

[22] L. Casetti, M. Pettini, E. G. D. Cohen, Geometric approach to Hamiltonian dynamics and statistical mechanics, Phys. Rep. 337 (2000) 237–341.

[23] G. Manfredi, R. O. Dendy, Test-Particle Transport in Strong Electrostatic Drift Turbulence with Finite Larmor Radius Effects, Phys. Rev. Lett. 76 (1996) 4360–4363.

[24] V. Naulin, K. H. Spatschek, Nonlinear drift-wave structures and their influence on particle transport, Phys. Rev. E 55 (5) (1997) 5883–5893.

[25] V. Naulin, A. H. Nielsen, J. J. Rasmussen, Dispersion of ideal particles in a two-dimensional model of electrostatic turbulence, Phys. Plasmas 6 (12) (1999) 4575–4585.

[26] R. Basu, T. Jessen, V. Naulin, J. J. Rasmussen, Turbulent flux and the diffusion of passive tracers in electrostatic turbulence, Phys. Plasmas 10 (7) (2003) 2696–2703.

[27] R. J. McKay, K. G. McClements, A. Thyagaraja, L. Fletcher, Test-particle simulations of collisional impurity transport in rotating spherical tokamak plasmas, Plasma Phys. Control. Fusion 50 (2008) 065017.

[28] Y. Sarazin, P. Ghendrih, Intermittent particle transport in two-dimensional edge turbulence, Phys. Plasmas 5 (12) (1998) 4214–4228.

[29] P. Ghendrih, Y. Sarazin, G. Attuel, S. Benkadda, P. Beyer, G. Falchetto, C. Figarella, X. Garbet, V. Grandgirard, M. Ottaviani, Theoretical analysis of the influence of external biasing on long range turbulent transport in the scrape-off layer, Nucl. Fusion 43 (2003) 1013–1022.

[30] R. Marchand, Test-Particle Simulation of Space Plasmas, Commun. Comput. Phys. 8 (3) (2010) 471–483.

[31] D. A. D'Ippolito, J. R. Myra, J. Zweben, Convective transport by intermittent blob-filaments: Comparison of theory and experiment, Phys. Plasmas 18 (2011) 060501.